

Variational multi-task MRI reconstruction: joint reconstruction, registration and super-resolution

Veronica Corona^{a,*}, Angelica Aviles-Rivero^a, Noémie Debroux^c, Carole Le Guyader^d, Carola-Bibiane Schönlieb^{a,*}

^aDepartment of Applied Mathematics and Theoretical Physics, University of Cambridge, UK

^bDepartment of Pure Mathematics and Mathematical Statistics, University of Cambridge, UK

^cUniversité Clermont Auvergne, CNRS, SIGMA Clermont, Institut Pascal, F-63000 Clermont-Ferrand, France

^dNormandie Université, INSA de Rouen, France

Abstract

Motion degradation is a central problem in Magnetic Resonance Imaging (MRI). This work addresses the problem of how to obtain higher quality, super-resolved motion-free reconstructions from highly undersampled MRI data. In this work, we present for the first time a variational multi-task framework that allows joining three relevant tasks in MRI: reconstruction, registration and super-resolution. Our framework takes a set of multiple undersampled MR acquisitions corrupted by motion into a novel multi-task optimisation model, which is composed of an L^2 fidelity term that allows sharing representation between tasks, super-resolution foundations and hyperelastic deformations to model biological tissue behaviors. We demonstrate that this combination yields significant improvements over sequential models and other bi-task methods. Our results exhibit fine details and compensate for motion producing sharp and highly textured images compared to state of the art methods while keeping low CPU time. Our improvements are appraised on both clinical assessment and statistical analysis.

Keywords:

2000 MSC: 92C50, 92C55, 94A08, 65K10, 49M37 MRI Reconstruction, Image Registration, Super-resolution, Motion Correction

1. Introduction

Magnetic Resonance Imaging (MRI) is a widely used and non-invasive modality that creates detailed images of the anatomical structures of the human body, including undergoing physiological events. It allows radiologists to examine MRI for diagnosis, treatment monitoring and abnormality/disease detection (Brown et al., 2015). However, a central limitation of MRI is the prolonged acquisition period needed to reconstruct an image (Zaitsev et al., 2015). This constraint is reputed to be a major contributor

to image quality degradation, and therefore, compromising the expert interpretation.

Image degradation appears as motion artefacts including blurring effects and geometric distortions (Sachs et al., 1995; Zaitsev et al., 2015). Therefore, the problem of how to reduce the acquisition time whilst producing high quality images, super-resolved and motion-free, is of a great interest in the community, and it is the problem that we address in this paper.

In particular, in a dynamic MRI setting, acquisitions with low signal-to-noise ratios or small anatomical structures might be severely degraded, affecting the final expert's outcome (Havsteen et al., 2017). These small structures can appear smeared or blurred, and discerning whether these are artefacts or lesions is very challenging

*Corresponding author:

Email addresses: vc324@cam.ac.uk (Veronica Corona), cbs31@cam.ac.uk (Carola-Bibiane Schönlieb)

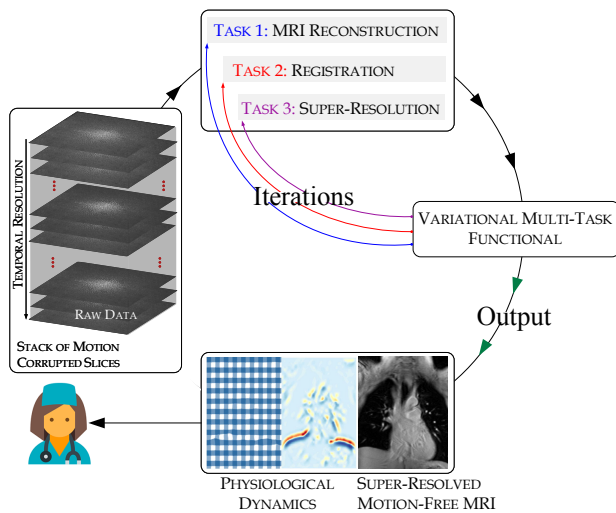


Figure 1: The proposed variational multi-task framework. A set of highly undersampled MRI measurements are taken as input to our three-task framework: reconstruction, registration and super-resolution. We then jointly address them using a proposed functional that has as output a super-resolved motion-free MRI that is structurally a statistically meaningful representative of the input data and the physiological dynamics.

for the expert, leading to potential false positive or negative findings (Andre et al., 2015). Moreover, movement distortions are most prominent at contrast edges (Birn et al., 2004).

Although it is possible to reduce the artefacts by performing breath-holding techniques, there is still residual motion to be compensated. This is mainly produced because the timescale of physiological motion is shorter than the required time to form an image. Likewise, gating strategies (Setser et al., 2000; Plein et al., Kaji et al., 2001; George et al., 2006; Jiang, 2006; Keall et al., 2000), which track either the breathing or cardiac cycles, have been also widely explored. However, they are mainly effective for perpetual breathing motion disregarding all other involuntary physiological motion and therefore only partially accurate. Furthermore, it is challenging to precisely co-register these signals to the corresponding MRI data (Hoisak et al., 2006).

As an alternative to the aforementioned techniques, a body of research has developed several algorithmic approaches based on the conceptual definition of Compressed Sensing (CS) which has demonstrated promising

results since the seminal paper of Lustig et al. (Lustig et al., 2007). The main idea of using CS is to reconstruct signals from low-dimensional measurements through iterative optimisation relying on the sparsity of the image in a transformed domain. Since then, several promising results have been reported in the body of literature e.g. (Liang, 2007; Lingala et al., 2011a,b; Otazo et al., 2015; Zhang et al., 2015). However, there is still a need for improving the quality of the MRI reconstruction whilst decreasing the number of measurements.

A commonality of previous techniques is that they perform a single task (just reconstruction). For a detailed survey in classic and machine learning methods for image reconstruction, we refer the reader to (Ravishankar et al., 2019). However, in most recent years, there has been a great interest for improving medical image reconstruction (Lingala et al., 2015; Royuela-del Val et al., 2016; Aviles-Rivero et al., 2018) by using what is called multi-tasking models (also known as joint models). The central idea of this perspective is that by sharing representation between tasks and carefully intertwining them, one can create synergies across challenging problems and reduce error propagation, which results in boosting the accuracy of the outcomes whilst achieving better generalisation capabilities.

Following the multi-task perspective, different works have been presented e.g. (Lingala et al., 2015; Royuela-del Val et al., 2016; Odille et al., 2016; Aviles-Rivero et al., 2018; Blume et al., 2010; Jacobson and Fessler, 2003). Unlike existing approaches from the literature, and to the best of our knowledge, we are presenting for the first time a model that considers more than two tasks i.e. bi-task models. In this work, we introduce a new variational multi-tasking framework that integrates, in a single model, three relevant tasks in MRI: reconstruction, registration and super-resolution (see Fig. 1). We remark that the ultimate goal of our three-task model is to improve the quality of the image reconstruction. Whilst this is a relevant part of this work, our contributions are:

- We propose a computationally tractable and mathematically well-motivated variational multi-task framework for MRI reconstruction, in which our novelties largely rely on:
 - An original optimisation model that is composed of an L^2 fidelity term that allows shar-

ing representations between three tasks (reconstruction, super-resolution and registration); a weighted total variation (wTV) ensuring the robustness of our method to intensity changes; a TV regulariser of the highly resolved reconstruction; and a hyperelasticity-based regulariser. We demonstrate that this combination yields significant improvements over sequential models and existing multi-task methods.

- We show that our optimisation problem can be solved efficiently by using auxiliary variables and then splitting it into sub-problems. We show that this requires lower CPU time than several methods from the body of literature.
- We extensively evaluate our approach using five datasets and different acceleration factors. We also compare our multi-task framework against existing approaches. Our experiments are further validated by interpretations of experts.

2. Related work

There have been different attempts to improve motion correction in MRI from undersampled data. Besides motion prevention techniques such as breath-holding, another set of algorithmic approaches has been devoted to correct motion using image-based motion tracking, where one needs an explicit estimation of the motion in between scans. The predominant scheme, in this context, is image registration which aims at finding a mapping aligning a moving image to a reference one. Following this perspective, the body of literature can be roughly classified into rigid (translations, rotations) and deformable registration.

In the first category, several approaches have been proposed including (Gupta et al., 2003; Adluru et al., 2006; Wong et al., 2008; Johansson et al., 2018). However, physiological motion such as cardiac and respiratory ones, can hardly be characterised by a simple combination of rotations and translations. To mitigate this limitation, motion correction methods based on deformable registration have been proposed such as (Ledesma-Carbayo MJ, 2007; Ledesma-Carbayo et al., 2007; Li et al., 2015; Jansen et al., 2017). However, in a closer look on the aforementioned approaches, a commonality between

them is that the algorithmic approaches are performed sequentially. That is - the motion estimation task is executed only after the image reconstruction is computed (from now we refer to this perspective as sequential model). A clear drawback of using this perspective is that the motion estimation highly depends on the quality of the reconstruction as well as on the selection of the reference image.

Another line of search has focused on solving jointly multiple tasks (the so-called multi-task approach) such as image reconstruction and registration in a unified framework. In particular, in the medical domain and following a variational perspective (Burger et al., 2018), different works have been reported using multi-task approaches. These include SPECT imaging (Mair et al., 2006; Schumacher et al., 2009), PET (Blume et al., 2010) and MRI (Lingala et al., 2015; Royuela-del Val et al., 2016; Aviles-Rivero et al., 2018) - to name a few.

The works with closer relations to ours are discussed next. In the context of MRI, authors of that (Royuela-del Val et al., 2016) introduced the GW-CS model, which addresses the reconstruction and registration problem. That model consists of alternating the resolution of a motion estimation problem relying on group-wise free-form registration using B-splines, and a motion-corrected compressed sensing MRI reconstruction step.

Authors in (Jacobson and Fessler, 2003) and (Blume et al., 2010) proposed a joint model composed of a motion-aware likelihood function and a smoothing term for a simultaneous image reconstruction and motion estimation for PET data. Schumacher et al. (Schumacher et al., 2009) presented an algorithmic approach that combines reconstruction and motion correction for SPECT imaging. The authors proposed a variational approach that includes a regulariser penalising an offset of motion parameter - to favour a mean location of the target object. However, the major limitation is that they only consider rigid motions. In the same spirit, authors of (Chun and Fessler; Fessler, 2010) proposed a generic joint reconstruction/registration framework. That model is based on a penalised-likelihood functional, which uses a weighted least square fidelity term along with a spatial and a motion regulariser.

Authors in (Odille et al., 2016) proposed a joint model for MRI image reconstruction and motion estimation. This approach allows for an estimate of both intra and

inter-image motion, meaning that, not only the misalignment problem is addressed but also it allows correcting for blurring/ghosting artefacts. Also with applications to MRI, authors of that (Lingala et al., 2015) proposed the Deformation Corrected - Compressed Sensing (DC-CS) model. This approach is based on a unified optimisation problem that combines a compressed sensing based reconstruction term along with a Demons registration method.

More recently in the context of deep-learning (DL), a number of methods have been investigated for image registration - e.g. (Yang et al., 2017; de Vos et al., 2017). Although, certainly, those approaches deserve attention, their review goes beyond the scope of this paper.

Super-resolution is considered as another fundamental task in MRI. This is mainly because it is another alternative to solve the central problem in MRI - to reduce the acquisition time, in which one seeks to recover a high resolved image from low resolution acquisitions. The potential of this task has been demonstrated since early works such as (Peled and Yeshurun, 2001; Greenspan et al., 2002). It continues being a focus of attention, which has been explored alone (Scheffler, 2002; Carmi et al., 2006; Zhang et al., 2007; Plenge et al., 2012; Odille et al., 2015; Chaudhari et al., 2018) or in a multi-task framework (Yue et al., 2016; He et al., 2007) with applications to MRI (Fogtman et al., 2012; Rousseau et al., 2006).

3. Proposed method

In this section, we introduce our joint variational framework which addresses simultaneously the following three tasks: MRI reconstruction, registration and super-resolution. We introduce the mathematical formulation as separate tasks and then we show how our novel optimisation model judiciously intertwines them. Finally, we describe the numerical realisation of our approach.

Why a three-task model? The motivation of our model comes from how we learn. That is- we use knowledge from other tasks to accelerate the learning process in a new task. An analogy to this observation is the basis for our multi-task approach, by optimising over multiple tasks, knowledge can be further shared to improve the MRI reconstruction.

How to select the three tasks? Our three tasks are selected based on the fundamental problem of MRI - how to reduce the acquisition time whilst having high quality images. Therefore, we have as a basic task the MRI reconstruction problem. For the second task, motion estimation is a well-known related task to MRI reconstruction e.g. (Sachs et al., 1995; Zaitsev et al., 2015). This is mainly because, since early developments, it has been shown that MRI is highly sensitive to motion. Our third task is super-resolution, it plays a crucial role in MRI since it is a form of trade-off to decrease the acquisition time. In other words, the fundamental problem of decreasing acquisition time in MRI can be solved through super-resolution, in which one seeks to have a high resolved image from low resolution acquisitions. This has motivated the development of different super-resolution approaches since early works in the area e.g. (Peled and Yeshurun, 2001; Greenspan et al., 2002).

Problem statement. We point out to the reader the focus of this work. Given a set of multiple undersampled MR acquisitions $\{x_t\}_{t=1}^T$ of low resolution and corrupted by motion, we seek to recover a single high resolved, static and motion-corrected image that represents the true underlying anatomy along with the estimation of the physiological dynamics through deformation maps.

3.1. Task 1: CS MRI Reconstruction

In particular, in standard dynamic MRI, the acquired data is in a time-spatial-frequency space, i.e. k, t -space, which is composed of $x = (x_{m,t})_{m=1,t=1}^{M,T} \in \mathbb{C}^{M \times T}$ measurements, where m is the spatial coordinate and t the temporal one. Therefore, the task of MRI reconstruction from those samples, reads:

$$x = \mathcal{A}u + \eta, \quad (1)$$

where $\mathcal{A}: \mathbb{R}^{N \times T} \rightarrow \mathbb{C}^{M \times T}$ is the undersampled MRI forward operator. More precisely, $\mathcal{A} = \mathcal{S}\mathcal{F}$ where \mathcal{S} is a subsampling operator, \mathcal{F} the Fourier operator, and $\mathcal{A}^*: \mathbb{C}^{M \times T} \rightarrow \mathbb{R}^{N \times T}$ its adjoint. Moreover, $u \in \mathbb{R}^{N \times T}$ is the stack of reconstructed images, η an additive Gaussian noise inherent to the acquisition, and t the temporal coordinate. Indeed, in this work we follow the standard assumption (Gudbjartsson and Patz, 1995; Ehrhardt and Betcke, 2016) according to which in most of the applications we have negligible phase, i.e. we are working with real valued, non-negative magnitude images.

The MRI reconstruction task is thus highly ill-posed due to the noise and incomplete measurements. However, (1) can be solved by adding prior information and then casting the problem as a CS-based optimisation problem:

$$u^* \in \arg \min_u \frac{1}{2} \| \mathcal{A}u - x \|_2^2 + \delta \| \Phi(u) \|_1, \quad (2)$$

where the first term, i.e. data fidelity term, ensures consistency with the observed data x whilst $\| \cdot \|_1$ enforces sparsity in the transformed domain given by Φ , and δ is a parameter balancing the influence of each term.

In this work, we focus on the Total Variation (TV) (Rudin et al., 1992) regulariser, which, imposing edge sparsity, leads to piecewise constant reconstructions. It has shown great potential since early developments in MRI reconstruction (Lustig et al., 2007).

Although a large body of literature has shown potential results in the context of undersampled MRI reconstruction using CS or its extended philosophies including (Lingala et al., 2011a; Majumdar and Ward, 2012; Otazo et al., 2015), there is still room for improvement, and in particular for the problem of reconstructing a single high quality image that reflects the true underlying anatomy. This motivates the use of two more tasks – image registration and super-resolution, which are described next.

3.2. Task 2&3: When Image Registration Meets Image Super-Resolution

In a dynamic MRI setting, there are two tasks that show a natural strong correlation: motion estimation and super-resolution. Therefore, our hypothesis is that by unifying these two tasks, one can create synergies leading to error propagation reduction, and therefore, an increase of the image quality.

In a multi-frame variational framework, super-resolution is the problem of restoring a high-resolution image from several low quality images that are corrupted by motion. From a variational perspective, it can be expressed as:

$$\min_u \sum_{i=1}^M \frac{1}{2} \| \text{DBW}_i u - f_i \|_2^2 + \lambda \text{Reg}(u), \quad (3)$$

where D and B are the downsampling and blurring operators correspondingly. Moreover, W_i models the geometric

warp existing between the observed images f_i and the restored image u to correct for motion. Finally, $\text{Reg}(u)$ is a generic regulariser. In this work, the downsampling operator is modelled as an averaging window, the blurring kernel is assumed to be Gaussian, and the warping operator is viewed as the deformations from a registration task. Whilst for the regulariser we adopt the TV option, one can easily replace the TV regulariser with other options.

In particular, for our registration method we have the following. Let Ω be the image domain, i.e. a connected bounded open subset of \mathbb{R}^2 , and $u: \Omega \rightarrow \mathbb{R}$ be the sought single reconstructed image depicting the true underlying anatomy. We introduce the unknown deformations, between the t -th acquisition and the image u , as $\phi_t: \bar{\Omega} \rightarrow \mathbb{R}^2$. We remark that the deformations are smooth mappings with topology preserving and injectivity properties. Moreover, let v_t be the associated displacements such that $\phi_t = \text{Id} + v_t$, where Id is the identity function. At the practical level, these deformations should be with values in $\bar{\Omega}$, and Ball’s results (Ball, 1981) guarantee this property theoretically for our model. We also consider $\nabla \phi_t: \Omega \rightarrow \mathbb{R}^{2,2}$ to be the gradient of the deformation, where $\mathbb{R}^{2,2}$ is the set of real square matrices of order two.

As MRI images biological soft tissues that are well-modelled by hyperelastic materials, we propose to view the shapes to be matched in the registration process as isotropic, homogeneous and hyperelastic materials of Ogden type. This choice allows for large and smooth deformations while keeping an elastic behavior. This is reflected in our formulation as a regularisation on the deformations ϕ_t based on the stored energy function of such materials.

In two dimensions, the stored energy function of an Ogden material, in its general form, is given by the following expression: $W_O(\nabla \phi) = \sum_{i=1}^P a_i \| \nabla \phi \|_F^{\gamma_i} + \Gamma(\det \nabla \phi)$, with $a_i > 0$, $\gamma_i \geq 1$ for all $i = 1, \dots, P$ and $\Gamma:]0; \infty[\rightarrow \mathbb{R}$ a convex function satisfying $\lim_{\delta \rightarrow 0^+} \Gamma(\delta) = \lim_{\delta \rightarrow +\infty} \Gamma(\delta) = +\infty$, $\| \cdot \|_F$ designating the Frobenius matrix norm.

Following (Corona et al., 2019), we consider the particular energy:

$$W_{Op}(\nabla \phi) = \begin{cases} a_1 \| \nabla \phi \|_F^4 + a_2 \left(\det \nabla \phi - \frac{1}{\det \nabla \phi} \right)^4 & \text{if } \det \nabla \phi > 0, \\ +\infty & \text{otherwise,} \end{cases} \quad (4)$$

with $a_1 > 0$, and $a_2 > 0$. Both changes in length and area are penalised and topology preservation is ensured with this formulation. The density W_{Op} is polyconvex since it can be written under the form $W_{Op}(F) = \mathbb{W}(F, \det F)$ with $\mathbb{W} : \mathbb{R}^{2,2} \times \mathbb{R} \rightarrow \bar{\mathbb{R}}$ a convex function. This writing yields fine properties.

3.3. Variational Multi-Task Model: Reconstruction, Registration and Super-Resolution

In the body of literature, there have been different attempts to use reconstruction, registration and super-resolution. However, they tackled the tasks either separately or jointly but up to two tasks. In this part, we describe, for the first time, how these three tasks can be jointly computed to benefit the final reconstruction. The main idea is to exploit temporal redundancy in the data to compensate for motion artefacts due to breathing, cardiac and/or involuntary movements whilst increasing the resolution to retrieve finer details in the reconstruction. In particular, we now turn to describe how (2) and (3) can be solved in a multi-task framework. From now on, \mathcal{A} is acting on a single frame meaning that contrary to the operator introduced in (1), \mathcal{A} is now defined on \mathbb{R}^N .

Our variational multi-task framework takes three key factors: firstly the hyperelastic regulariser (4), secondly a discrepancy measure that joins the reconstruction, super-resolution and the registration tasks, and the TV-based regularisers for reconstruction and super-resolution. Moreover, our model accounts for intensity changes, this, by modifying the CS-classical TV regulariser for the weighted TV to enforce edge alignment (see Definition in Appendix D). In this way, we are able to make our model more robust with respect to intensity changes that often occur when acquiring multiple frames. From now on, \mathcal{A} is acting on one single frame. We thus introduce weights g_t as the Canny edge detector applied to $G_\sigma * \mathcal{A}^* x_t$ - for each $t = 1, \dots, T$ - where G_σ is a Gaussian filter of variance σ .

We thus consider the following fidelity term and regulariser for our high-resolved image:

$$E(u, (\phi_t)_{t=1, \dots, T}) = \alpha \text{TV}(u) + \frac{1}{T} \sum_{t=1}^T \left(\delta \text{TV}_{g_t}((Cu) \circ \phi_t^{-1}) + \frac{1}{2} \|\mathcal{A}((Cu) \circ \phi_t^{-1}) - x_t\|_2^2 \right), \quad (5)$$

where $C = DB$ comes from the super-resolution formulation. The second term of E seeks to align the edges of the deformed reconstruction $((Cu) \circ \phi_t^{-1})$ with the ones of the different acquisitions, whilst regularising it. The last quantity aims to get $\mathcal{A}((Cu) \circ \phi_t^{-1})$ close to the acquisitions x_t , and thus $\mathcal{A}^*(x_t)$ close to $Cu \circ \phi_t^{-1}$ to correct for motion.

Our variational multi-task framework is then defined as a combination of (4) and (5), which leads to the following minimisation problem:

$$\begin{aligned} \inf_{u, (\phi_t)_{t=1, \dots, T}} \mathcal{G}(u, (\phi_t)_{t=1, \dots, T}) &= E(u, (\phi_t)_{t=1, \dots, T}) \\ &+ \frac{1}{T} \sum_{t=1}^T \int_{\Omega} W_{Op}(\nabla \phi_t) \, dx, \\ \Leftrightarrow \inf_{u, (\phi_t)_{t=1, \dots, T}} \alpha \text{TV}(u) &+ \frac{1}{T} \sum_{t=1}^T \left(\frac{1}{2} \|\mathcal{A}((Cu) \circ \phi_t^{-1}) - x_t\|_2^2 \right. \\ &\left. + \delta \text{TV}_{g_t}((Cu) \circ \phi_t^{-1}) + \int_{\Omega} W_{Op}(\nabla \phi_t) \, dx \right), \end{aligned} \quad (6)$$

We now introduce the next theorem to set the well-posedness of our model.

Theorem 1 (Existence of minimisers). *Let $\mathcal{A} = \mathcal{S}\mathcal{F} : L^2(\mathbb{R}^2) \rightarrow L^2(\mathbb{R}^2)$, $C : L^1(\Omega') \rightarrow L^p(\Omega)$, be linear bounded and continuous for the strong topology operators with $p \in]1, \frac{8}{5}[$, and $\Omega \subset \Omega'$, Ω and Ω' connected bounded open subsets of \mathbb{R}^2 with boundaries of class C^1 (verified by the chosen operators). We assume that $g_t : \mathbb{R}^+ \rightarrow \mathbb{R}^+$, $g_t(0) = 1$, g_t is strictly decreasing, $\lim_{r \rightarrow +\infty} g_t(r) = 0$, and there exists $c > 0$ such that $c \leq g_t \leq 1$ everywhere (verified by the chosen ones). With $\delta, \alpha, a_1, a_2 > 0$, problem (6) admits minimisers $(\bar{u}, (\bar{\phi}_t)_{t=1, \dots, T})$ on $\mathcal{U} = \{u \in BV(\Omega'), \phi_t \in \mathcal{W}, \forall t = 1, \dots, T \mid (Cu) \circ \phi_t^{-1} \in BV_{g_t, 0}(\Omega), \forall t \in \{1, \dots, T\}\}$, with $\mathcal{W} = \{\psi \in Id + W_0^{1,4}(\Omega, \mathbb{R}^2) \mid \det \nabla \psi \in L^4(\Omega), \frac{1}{\det \nabla \psi} \in L^4(\Omega), \det \nabla \psi > 0 \text{ a.e. on } \Omega\}$, Id being the identity map meaning that the deformations are equal to the identity on the boundaries.*

The proof can be found in Appendix D.

In the next section, we detail how the proposed model (6) can be solved in a computational tractable form.

3.4. Optimisation Scheme

The numerical realisation of (6) imposes different challenges due to the nonlinearity and nonconvexity in $\nabla\phi_t$ and the composition $(Cu) \circ \phi_t^{-1}$ in the fidelity term. In this work, we overcome these difficulties by introducing three auxiliary variables z_t, h_t, f_t , this, to mimic $\nabla\phi_t, (Cu) \circ \phi_t^{-1}$ and h_t . We then relax our problem using quadratic penalty terms modified to facilitate the change of variables required for the computations. This leads to the following discretised decoupled problem:

$$\begin{aligned} \min_{u, \phi_t, z_t, h_t, f_t} & \alpha \text{TV}(u) + \frac{1}{T} \sum_{t=1}^T \sum_{x \in \Omega} \left(W_{Op}(z_t(x)) \right. \\ & + \frac{\gamma_1}{2} \|z_t - \nabla\phi_t\|_2^2 + \frac{\gamma_3}{2} \|\mathcal{A}h_t - x_t\|_2^2 \\ & + \frac{\gamma_2}{2} \|(h_t - (Cu) \circ \phi_t^{-1}) \sqrt{\det \nabla(\phi_t^{-1})}\|_2^2 \\ & \left. + \frac{\gamma_4}{2} \|f_t - h_t\|_2^2 + \delta \text{TV}_{g_t}(f_t) \right). \end{aligned} \quad (7)$$

We now can solve our minimisation problem by splitting (7) into five more computational tractable sub-problems. We now turn to give more details on each sub-problem.

● **SUB-PROBLEM 1: OPTIMISATION OVER z_t .** In practice, $z_t = (z_{t,1}, z_{t,2})^\top$ simulates the gradient of the displacements $v_t = (v_{t,1}, v_{t,2})^\top$ associated to the deformations ϕ_t . For every z_t , we have $z_t = \begin{pmatrix} z_{11} & z_{12} \\ z_{21} & z_{22} \end{pmatrix}$. For the sake of readability, we drop here the dependency on t . We solve the Euler-Lagrange equation with an L^2 gradient flow and a semi-

implicit finite difference scheme and update z_t as:

$$\begin{aligned} z_{11}^{k+1} &= \frac{1}{1 + dt\gamma_1} \left(z_{11}^k + dt(-4a_1\|I + z_t^k\|_F^2(z_{11}^k + 1) \right. \\ & \quad \left. - 4a_2(1 + z_{22}^k)c_0c_1 + \gamma_1 \frac{\partial v_{t,1}^k}{\partial x} \right), \\ z_{12}^{k+1} &= \frac{1}{1 + dt\gamma_1} \left(z_{12}^k + dt(-4a_1\|I + z_t^k\|_F^2 z_{12}^k \right. \\ & \quad \left. + 4a_2z_{21}^k c_0c_1 + \gamma_1 \frac{\partial v_{t,1}^k}{\partial y} \right), \\ z_{21}^{k+1} &= \frac{1}{1 + dt\gamma_1} \left(z_{21}^k + dt(-4a_1\|z_t^k + I\|_F^2 z_{21}^k \right. \\ & \quad \left. + 4a_2z_{12}^k c_0c_1 + \gamma_1 \frac{\partial v_{t,2}^k}{\partial x} \right), \\ z_{22}^{k+1} &= \frac{1}{1 + dt\gamma_1} \left(z_{22}^k + dt(-4a_1\|I + z_t^k\|_F^2(z_{22}^k + 1) \right. \\ & \quad \left. - 4a_2(1 + z_{11}^k)c_0c_1 + \gamma_1 \frac{\partial v_{t,2}^k}{\partial y} \right), \end{aligned} \quad (8)$$

with $c_0 = (\det(I + z_t^k) - \frac{1}{\det(I + z_t^k)})^3$ and $c_1 = 1 + \frac{1}{(\det(I + z_t^k))^2}$ and I being the identity matrix. The step size dt was set to 0.01.

● **SUB-PROBLEM 2: OPTIMISATION OVER ϕ_t .** We solve the Euler-Lagrange equation in ϕ_t , after making the change of variable $y = \phi_t^{-1}(x)$ in the L^2 penalty term, for all t , using an L^2 gradient flow scheme with a semi-implicit Euler time stepping.

$$\begin{aligned} 0 &= -\gamma_1 \Delta \phi_t^{k+1} + \gamma_1 \begin{pmatrix} \text{div } z_{t,1}^{k+1} \\ \text{div } z_{t,2}^{k+1} \end{pmatrix} \\ & \quad + \gamma_2 (h_t^k \circ \phi_t^k - Cu^k) \nabla h_t^k(\phi_t^k). \end{aligned} \quad (9)$$

● **SUB-PROBLEM 3: OPTIMISATION OVER h_t .** The update in h_t , for all t , has a closed form solution using the subsampling operator \mathcal{S} and the Fourier operator \mathcal{F} along with

their adjoints \mathcal{S}^* and $\mathcal{F}^* = \mathcal{F}^{-1}$:

$$h_t^{k+1} = \mathcal{F}^* \left\{ (\gamma_2 \det \nabla(\phi_t^{-1})^{k+1} \mathbf{I} + \gamma_3 \mathcal{S}^* \mathcal{S} + \gamma_4 \mathbf{I})^{-1} \right. \\ \left. \left(\mathcal{F}(\gamma_2 \det \nabla(\phi_t^{-1})^{k+1} (Cu^k) \circ (\phi_t^{-1})^{k+1} + \gamma_4 f_t^k) \right. \right. \\ \left. \left. + \gamma_3 \mathcal{S}^* x_t \right) \right\}. \quad (10)$$

• **SUB-PROBLEM 4: OPTIMISATION OVER f_t .** This is solved via Chambolle projection algorithm (Chambolle, 2004). For an inner loop over $n = 1, \dots, M$:

$$f_t^{n+1} = h_t^{k+1} - \frac{1}{\gamma_4} \delta \operatorname{div} p_t^n, \\ p_t^{n+1} = \frac{p_t^n + \tau \nabla(\operatorname{div} p_t^n - h_t^{k+1} \gamma_4 / (\delta))}{1 + \frac{\tau}{\delta} \|\nabla(\operatorname{div} p_t^n - h_t^{k+1} \gamma_4 / (\delta))\|}, \quad (11)$$

with $\|\cdot\|$ the Euclidean norm in \mathbb{R}^2 . After enough iterations, we set $f_t^{k+1} = f_t^{n+1}$.

• **SUB-PROBLEM 5: OPTIMISATION OVER u .** Finally, using the same change of variables as in sub-problem 2, the problem in u reads:

$$\min_u \frac{\gamma_2}{2T} \sum_{t=1}^T \|h_t \circ \phi_t - (Cu)\|_2^2 + \alpha \operatorname{TV}(u), \quad (12)$$

and we solve it with a primal-dual algorithm (Chambolle and Pock, 2011):

$$y^{k+1} = \frac{y^k + \sigma \nabla u^k}{\max(1, \|y^k + \sigma \nabla u^k\|)}, \\ u^{k+1} = \left(\frac{\gamma_2}{T} C^* C + \mathbf{I} \right)^{-1} \left(u^k + \tau \operatorname{div} y^{k+1} \right. \\ \left. + \frac{\gamma_2}{T} C^* \sum_{t=1}^T h_t^{k+1} \circ \phi_t^{k+1} \right). \quad (13)$$

We remark that, in this work, we solve the registration problem in z_t and ϕ_t in a multi-scale framework from coarser to finer grids and using a regriding technique (Christensen et al., 1996) (see Appendix A). The latter ensures topology preservation even though theoretically the design of the regulariser guarantees positivity of the Jacobian determinant.

4. Experimental results

In this section, we present the experimental results performed to validate our proposed approach.

4.1. Data Description

We evaluate our framework on five publicly available datasets.

- **Dataset 1, 2 & 3**¹ These datasets are 2D T1-weighted data (Baumgartner et al., 2017) acquired during free-breathing of the entire thorax. It was acquired with a 3T Philips Achieva system with matrix size = 215×173 , slice thickness=8mm, TR=3.1ms and TE=1.9ms, for 40 temporal frames. We remark that each dataset refers to three different patients.
- **Dataset 4 & 5**² The datasets are 4DMRI data acquired during free-breathing of the right liver lobe (von Siebenthal et al., 2007). It was acquired on a 1.5T Philips Achieva system using a T1-weighted gradient echo sequence, TR=3.1 ms, coils=4, slices=25, matrix size = 195×166 , over roughly one hour on 22 to 30 sagittal slices and a temporal resolution of 2.6 – 2.8 Hz.

In this paper, we consider Cartesian sampling.

4.2. Evaluation Protocol

To validate our theory, we extensively evaluate our model as follows.

Comparison against sequential models. For the first part of our evaluation, we compared our variational multi-task approach against two well-known models, *rigid* (RIGID), and *hyperelastic* (HYPER), for deformations. To run this comparison, we solve the CS reconstruction model with TV, and then register all the frames to a reference frame used as initialisation in our proposed approach. For this, we use the well-established FAIR toolbox (Modersitzki, 2009), where we select rigid and hyperelastic transformations. Finally, we perform the super-resolution task with TV.

¹<https://zenodo.org/record/55345#.XB0kvi2cbUZ>

²http://www.vision.ee.ethz.ch/~organmot/chapter_download.shtml

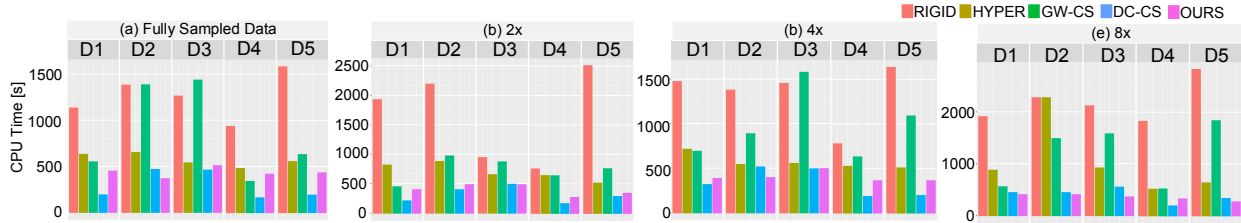


Figure 2: Computational performance comparison between sequential (three tasks), joint (two tasks) and our approach. Elapsed time in seconds. The sequential approaches are far slower than our proposed method. We can see that our approach is comparable and competitive with joint approaches although slightly slower than the DC-CS, which, however, only computes two tasks. We denote DN as the number of the dataset used where N correspond to the dataset number.

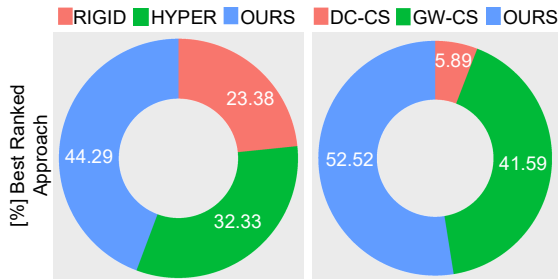


Figure 3: User study results (in %) indicating the level of agreement of clinicians for sequential and multi-task comparisons. The majority indicates that our proposed reconstructions ranked the best.

Comparison against other multi-task approaches.

As to the best of our knowledge, this is the first variational model joining three tasks, we compare our model against two models that only joint two tasks- reconstruction and the motion estimation. More precisely, we compared our method against DC-CS (Lingala et al., 2015) and GW-CS (Royuela-del Val et al., 2016). To show robustness and generalisation capabilities of our approach, we ran the comparisons using fully sampled data and acceleration factors = $\{2, 4, 5, 6, 8\}$.

Metrics evaluation. As we seek to recover a single high resolved and motion corrected image not corresponding to a specific initial frame, there is no ground truth for this task. Therefore, our evaluation is based on a standard protocol (Patel et al., 1994) for evaluating MRI reconstruction, that is a user-study (expert scoring). For this, we designed a three-point Likert rating scale in which experts were asked to indicate the level of agreement, ranging from *best reconstruction* to *worst recon-*

struction. Following standard protocol in user studies, we supported our study by a nonparametric statistical test. Detailed protocol can be found in [Appendix B](#). Moreover, to further support our multi-task model, we also offer CPU time comparison against all the compared approaches.

The experiments reported in this section were run under the same conditions in a CPU-based Matlab implementation. We used an Intel core i7 with 4GHz and a 16GB RAM.

4.3. Parameters Reasoning and Selection

In our experiments, we set the parameters of our approach and the compared ones as described next. For our experiments, we set the parameters as displayed in [Table 1](#). Whilst for the sequential approaches, based on the FAIR implementation, we set the hyperelastic regularisation parameters for Datasets 1, 2 & 3 = 1 and for Datasets 4 & 5 = 0.1. We remark that the results from FAIR toolbox have been produced under fair conditions by selecting an optimal parameter setting.

We discuss the influence of each parameter. The parameters a_1 and a_2 control the regularisation of the deformations. Whilst the former acts on the smoothness of the deformations, the latter can be seen as a measure of compressibility. That is- the bigger a_2 is, the more rigid the deformations are and the less accurate the registration becomes. It thus behaves as a compromising parameter between the ability to handle large and nonlinear deformations, and topology preservation.

Moreover, γ_1 , γ_2 and γ_4 are chosen to take large values, to ensure the closeness of the auxiliary variables to

	D1	D2	D3	D4	D5
a_1	1	1	1	1	1
a_2	50	50	50	100	100
γ_1	5	5	5	1	1
γ_2	10^5	10^5	10^5	10^5	10^5
γ_3	15	15	15	1	1
γ_4	0.2	0.2	0.2	0.2	0.2
σ	1.5	1.5	1.5	2	2
k	2	2	2	2	2
$N\&n$	500	500	500	500	500
α	0.01	0.01	0.01	0.001	0.001

Table 1: Parameter values used for our model and for all datasets. In this table, "D" stands for Dataset.

the original ones. The parameter γ_3 weights the fidelity term joining the three tasks, and it is often chosen to be close to 1. Finally, α offers a balance between regularity and fidelity to the data for the super-resolved reconstructed image u .

4.4. Results and Discussion

We evaluate our proposed approach following the scheme described in [Subsection 4.2](#).

► Is our multi-tasking approach better than a sequential one?

We start evaluating our approach against two sequential models. We point out to the reader that sequential means executing tasks (reconstruction, registration and super-resolution) one after another. In particular, we compared our approach against two well-known models for deformations: rigid (RIGID) and hyperelastic (HYPER). Results of this comparison are displayed in [Figs. 4](#) and [5](#), and using different acceleration factors.

In a closer look at those figures, one can see that our reconstructions have better sharp edges and retrieve finer details, in the heart and below the lung areas, than the sequential approaches. Particularly, the rigid transformation is not able to compensate for the whole motion and thus blurring effects are visible, especially under the lungs, for all acceleration factors. Hyperelastic deformations, however, have more degrees of freedom and are capable of better compensating for motion which is manifested by sharp edges in the HYPER reconstruction. Moreover, the

darker structure, at the center bottom of the heart, disappears or is much less visible in the HYPER reconstructions than in our approach. This effect is observed for all acceleration factors.

Besides, as the acceleration factor increases, the HYPER reconstruction loses the initial contrast, which is particularly visible for the acceleration factor of 8. In contrast, our multi-task framework is able to preserve it nicely. This shows the robustness of our method to noise and corrupted data. The benefit of our multi-task framework is prevalent to all datasets (see [Appendix C](#) for Dataset 2, 4 and 5).

[Figs. 4](#) and [5](#) show that hyperelastic deformations are better suited to deal with complex physiological motions. Indeed, the RIGID reconstructions exhibit strong blurring artefacts due to residual movements which are amplified as the acceleration factor increases. Also, our method is able to preserve small structures in the kidney and the white blood vessels in the liver even for large acceleration factors contrary to the sequential HYPER approach. For the acceleration factor of 8, the HYPER reconstruction suffers more from staircasing effects than our approach and loses the initial contrast.

Overall, we can show that sharing representation between tasks (i.e. our multi-task approach) leads to better MRI reconstructions than if one performs the tasks separately. This is strongly supported by two factors, the computational time and the expert agreement. Following common protocol for MRI evaluation, we performed a user-study, in which we asked twelve experts (radiologist trainees and experienced) to evaluate reconstructions with all acceleration factors in [Figs. 4](#) and [5](#) (see [Appendix C](#) for Datasets 2, 4 and 5).

The outcome is displayed in [Fig. 3](#). At left side of this figure, one can see that overall (i.e. for all reconstruction/all acceleration factors) our approach was ranked best, with a 44.29% of agreement, in comparison with the output from the other methods. We also ran the nonparametric Friedman test, per acceleration and therefore accounting for FDR (False Discovery Rate), and we found that there is significant statistical difference- that is, our approach offered the best reconstructions.

To further support our model performance, we also analyse the difference maps to assess the quality of our registration, and therefore, its motion correction potential. To do this, we inspect the uncorrected average of the

difference image, between a reference frame and each individual one, which is displayed at the left side of Fig. 6. From this column, we can observe that the motion is significant in both datasets. However, when we inspect the mean difference between our reconstruction and the individual registered acquisitions ($h_t \circ \phi_t$), at the middle and right sides of Fig. 6, one can see that the structures are very well-aligned resulting in a much smaller range in difference maps. Overall, our approach successfully corrects for motion even at low undersampling rates, and this effect is preserved for all datasets.

► **Is a three-task framework better than a two-task one?** In a multi-task framework, a key factor is to assess if the tasks are not affecting negatively the final MRI reconstruction. To evaluate this factor, we ran a set of experiments of our approach against two multi-task frameworks DC-CS (Lingala et al., 2015) and GW-CS (Royuela-del Val et al., 2016). These approaches perform only two tasks (reconstruction and estimation) and constitute our baselines as, to the best of our knowledge, there exists no approach joining three tasks. We remark that we refer to a two-task (bi-task) approach as: an approach that performs reconstruction and motion estimation. Whilst our three-task model is referred to the optimisation scheme that seeks to solve three tasks. In particular, our tasks are reconstruction, motion estimation (cast as an image registration task) and super-resolution. In our work, we further differentiate these models by those that perform the tasks: i) sequentially, that is- the motion estimation task is executed only after the image reconstruction is computed, and ii) in a multi-task form (jointly), that is- all the tasks are executed at the same time whilst sharing representations across tasks.

The MRI reconstruction from our model against DC-CS and GW-CS can be seen in Figs. 4 and 5 (see Appendix C for further visualisation with the remaining datasets). In a closer look at these figures, one can observe very blurred reconstructions from DC-CS, which can be interpreted as a failure of the model to capture the complex intrinsic nature of physiological motions. In contrast, GW-CS and our reconstructions are sharper even for very low undersampling factors and compensate well for motion.

However, our method is more robust to noise and outliers (as displayed in the compared reconstructions). Al-

though the GW-CS reconstructions preserve fine textures and small structures, they are noisier than ours. That is, our approach improves the quality in terms of preserving information whilst removing noise in comparison with GW-CS. This effect is elevated even more as the acceleration factor increases. For example, for an acceleration factor of 8, artefacts and noise are visible in the heart and under the lungs in the GW-CS reconstruction whereas ours is clearer.

Another example of the good performance of our approach can be seen in Fig. 5, in which we are able to retrieve more clinically useful texture and fine details than the GW-CS technique. This is particularly visible in the central part of the heart where noise is visible in the GW-CS reconstructions especially as the acceleration factor increases.

To further support our results, we display, at the right side of Fig. 3, the overall outcome of the user-study. From this plot, we can see that the majority of the experts agreed that our reconstructions are better than the compared approaches. Although the second best ranked is GW-CS, it fails to correct for noise which compromises the readability of the underlying texture. Moreover, as soon as the acceleration factor increases, the noise level jumps, reducing drastically the readability and interpretability of the GW-CS reconstructions whereas our method retrieves relevant small structures and denoises the reconstruction.

► **The CPU cost of our multi-tasking approach - does it pay off?** From previous sections, we demonstrated that our approach achieves a better reconstruction in comparison with other approaches, however, does this improvement come to pay off in terms of computational time? Therefore, in this section, we highlight the computational advantages of our model. We point out to the reader that all comparisons were run under the same conditions.

The CPU time, for all approaches, is displayed at Fig. 2 for several acceleration factors (the remaining can be found in Appendix C). Firstly, we observe that, in terms of sequential models, our model outperforms RIGID and HYPER reporting the lower CPU time. However and in terms of the other multi-task methods, the computational time for GW-CS is much longer compared to our method (and it only performs two tasks). Whilst the DC-CS approach readily competes with our approach from the image quality standpoint, our method offers by far better re-

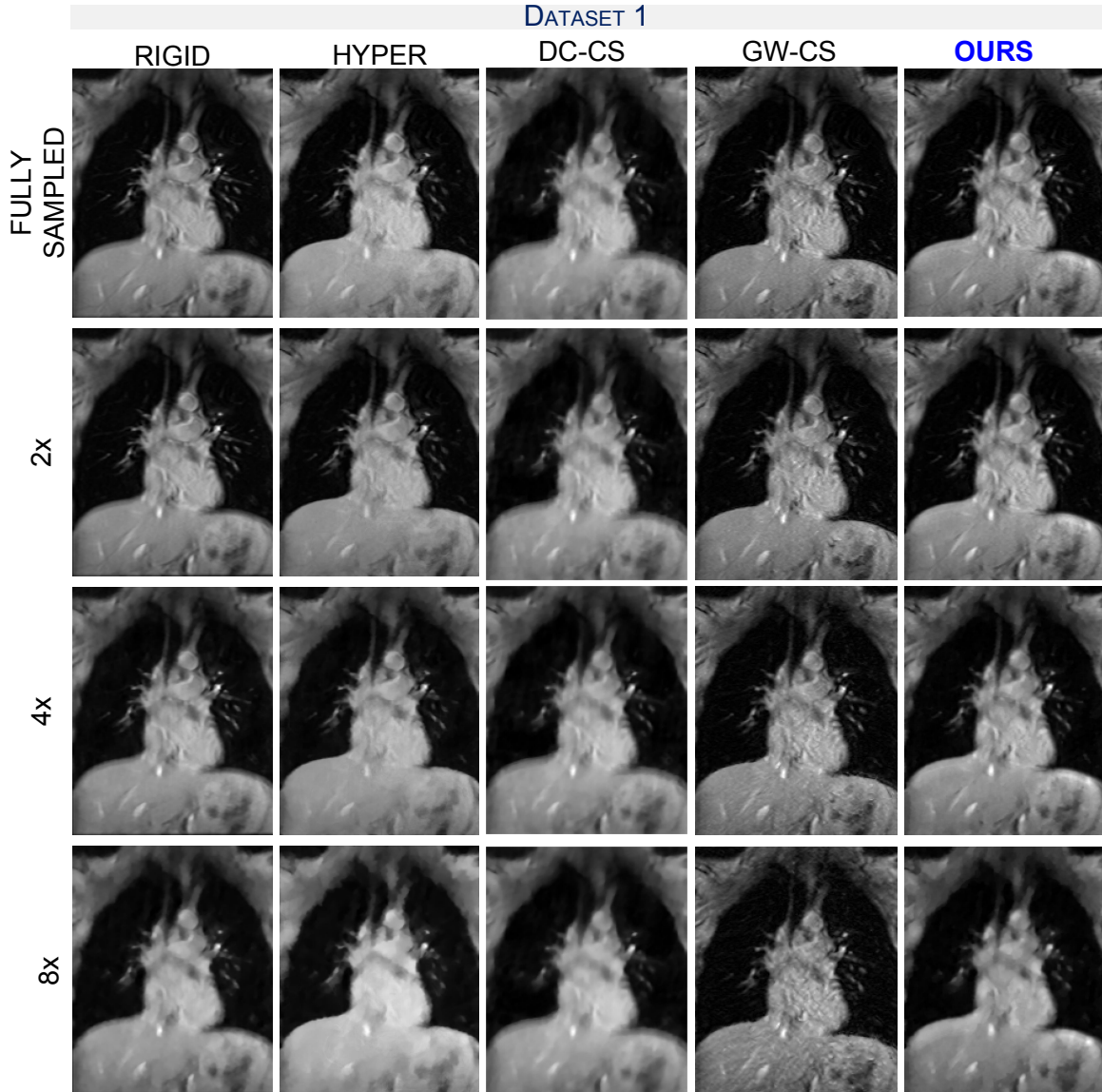


Figure 4: Reconstruction results for Dataset 1 for different acceleration factors and different joint approaches in comparison to our proposed method. We can clearly see that our approach provides the best results in terms of sharp structures and fine texture, while the compared techniques are more blurry and noisy than ours. This is particularly accentuated for high undersampling factors.

sults in terms of reconstruction. We emphasise that the CPU times for our model and DC-CS are still on the same range, but the proposed method is performing three tasks instead of two like the DC-CS. These advantages high-

light our optimisation scheme that allows computing a complex problem in a very computational tractable form.

Other options for our model construction. One can think in using $C(u \circ \phi_t^{-1})$ instead of $(Cu) \circ \phi_t^{-1}$. How-

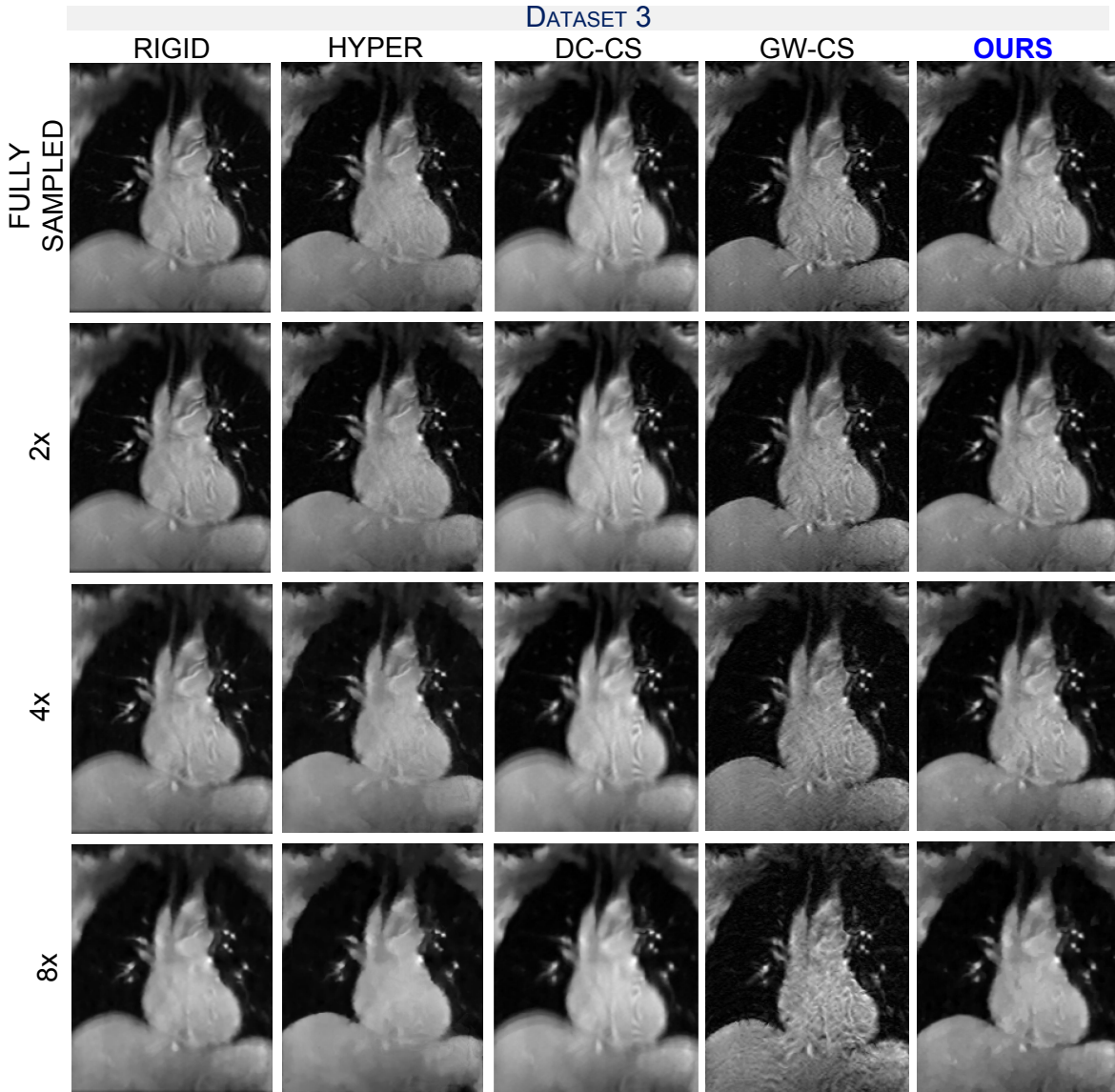


Figure 5: Comparison of our multi-task framework vs other single- and bi-task approaches on Dataset 3. We note that our approach can preserve fine details and sharp edges whilst the compared techniques yields to blurring artefacts. We can also note the GW-CS approach highly amplifies the noise. This is more visible for high undersampling factors.

ever, we noticed negligible performance gain in comparison with our current model. The main reason to choose our current model is the computational gain.

5. Conclusion

In this work we propose a novel variational multi-task framework to achieve higher quality and super-resolved reconstructions. Our method compensates for motion in

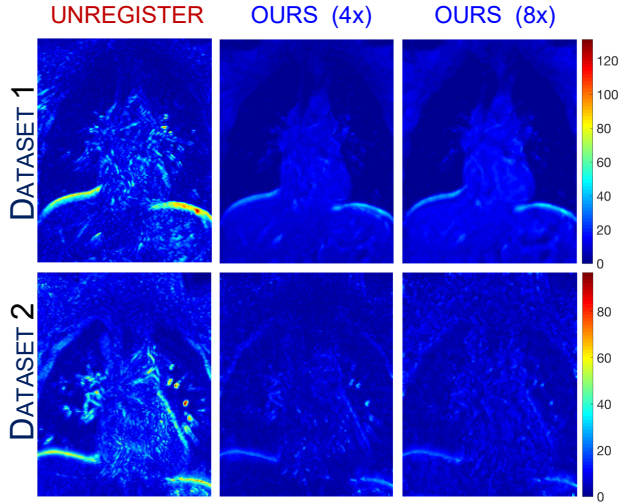


Figure 6: Difference maps. From left to right: average absolute difference maps of the unregistered sequence, average absolute difference maps of the corrected sequence for an acceleration factor of 4 and 8 and the colorbar for Datasets 1 and 2.

undersampled data. To the best of our knowledge, it is the first variational framework that allows computing three tasks jointly.

In particular, our multi-task framework is composed of four major components: an L^2 fidelity term intertwining MRI reconstruction, super-resolution and registration; a weighted TV ensuring robustness of our method to intensity changes by promoting edge alignment; a TV regulariser of the super-resolved reconstruction; and a hyperelasticity-based regulariser modelling biological tissue behavior and allowing for large and smooth deformations. We exploit the temporal redundancy to correct for blurring artefacts and increase image quality. As a result, we obtain a single highly resolved and clear image reconstruction representing the true underlying anatomy.

The advantages of our model is that we guarantee preservation of anatomical structures whilst keeping fine details and less blurry and noise artefacts in the final reconstructions. We extensively evaluate our method against sequential and other multi-task methods from the body of literature. We demonstrate that our method achieves the best results whilst demanding low CPU time. Our method is further supported by a user-study (experts).

Future Work. This multi-task framework is indeed

very well-suited for the plug-and-play setting when one (or more) imaging tasks could be replaced by different algorithms. For instance, the modelling of the regularisation functional for the high resolution image reconstruction could be replaced in a plug-and-play fashion. We remark that our method opens the door to both hybrid methods (i.e. model-based in combination with machine learning based methods) and fully end-to-end approaches. For example, a task in our model can be replaced by its counterpart in deep learning or even the full idea of a three-task model can be cast as an end-to-end deep learning model. Also, the work of Gris *et al.* [Gris et al. (2019)] dedicated to image reconstruction from noisy and indirect observations by registering a template via metamorphosis might motivate some future works authorising diffeomorphic changes to both the geometry of the template and its intensity values.

Acknowledgment

VC acknowledges the financial support of the Cambridge Cancer Centre and the Cambridge Research UK. CBS acknowledges support from the Leverhulme Trust project on ‘Breaking the non-convexity barrier’, EPSRC grant Nr. EP/M00483X/1, EP/S026045/1, the EPSRC Centre Nr. EP/N014588/1, the RISE projects CHiPS and NoMADS and the Alan Turing Institute. Support from the Centre for Mathematical Imaging in Healthcare, Cantab Capital Institute for the Mathematics of Information and the National Physical Laboratory are greatly acknowledged.

Appendix A. Parameters Reasoning of Our Multi-Task Framework

The parameters specified in the main Table 1 have been chosen after optimisation among the following ranges:

Finally, we also explicitly define the regridding algorithm that we used in [Subsection 3.4] of the main paper. This is displayed at Algorithm 1.

Appendix B. Further Details on the User-Study

In this section, we give further details on our user-study. We followed a common protocol for analysing responses

PARAMETER	RANGE
α_1	0.1, 0.5, 1, 2, 5, 10
α_1	10,20,30,50,70,100
γ_1	1,2,5,7,10
γ_2	$10^3, 10^4, 10^5, 10^5, 10^6, 10^7$
γ_3	0.1, 0.5, 1, 2, 5, 10,15,20,30
γ_4	$1, \frac{1}{2}, \frac{1}{5}, \frac{1}{10}$
σ	0.1,0.5,1,1.5,2,2.5
k	1:10
n	100,200,500
α	0.0001,0.001,0.01,0.1

Algorithm 1 Regridding algorithm

- 1: Initialisation $z^0 = 0, \phi^0 = \text{Id}, \text{regrid_count} = 0$ (variable which counts the number of regridding steps needed in the general algorithm).
 - 2: **for** $n = 1, \dots, N$ **do**
 - 3: Update z^n and ϕ^n .
 - 4: **if** $\det \nabla \phi^n < \text{tol}$ **then**
 - 5: $\text{regrid_count} = \text{regrid_count} + 1$.
 - 6: $h = h \circ \phi^{n-1}$.
 - 7: Save $\text{tab}_\phi(\text{regrid_count}) = \phi^{n-1}$, tab_ϕ is a table variable in which the successive deformations are stored in order to do the composition at the end of the process.
 - 8: $\phi^n = \text{Id}, z^n = 0$.
 - 9: **end if**
 - 10: **end for**
 - 11: **if** $\text{regrid_count} > 0$ **then**
 - 12: $\phi^{\text{final}} = \text{tab}_\phi(1) \circ \dots \circ \text{tab}_\phi(\text{regrid_count})$.
 - 13: **end if**
-

in survey research. To this aim, we used a Likert scale that measures the level of agreement of the expert/user. This prevented precisely the difficulty of drawing conclusions from open answers/opinions. Our user study was driven by the best way to capture the experts opinion from the psychological and statistical point of views - overall, we avoided subjectivity in the analysis by relying our results on a well-established psychometric scale (i.e. Likert scale).

To further support our results, we performed a user-study following standard protocol in clinical settings.

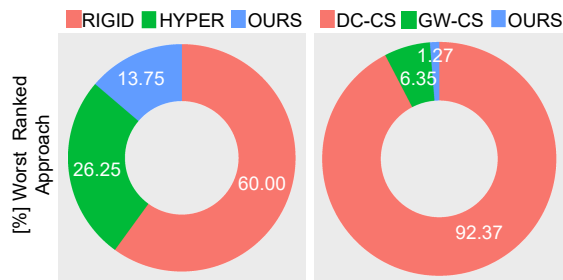


Figure B.7: Plots display the percentage of responses supporting the worst ranked approach.

That is- to ask twelve radiologists to evaluate the reconstructions based on a scoring system. The radiologists have more than 5 years of practice.

Scoring Procedure. We created an electronic survey in which, after giving the instructions to the users, they were provided with a two-part evaluation. For the first part, they evaluated the reconstructions related to sequential models. To do this, they were provided with the reconstructions of the five dataset, for acceleration factor = {fully sampled, 2x, 4x, 6x, 8x}, and for the approaches = {RIGID, HYPHER, OURS} (see main paper for description on these models). With the purpose of capturing their scores, we design a three-point Likert rating scale in which experts were asked to indicate the level of agreement, ranging from best reconstruction to worst reconstruction. Similarly, this protocol was followed to evaluate other multi-task methods = {DC-CS, GW-CS, OURS}. Fig. B.7 displays the results in terms of % of the worst ranked for all compared approaches.

Statistical Analysis. The circle plots displayed in the main paper and in Fig. B.7 of this appendix, reflects the averaged results of all scoring (i.e. for all acceleration and all reconstructions). However, to test if there was statistical significant difference between the approaches, we took into account the scoring per each reconstruction, and ran the nonparametric Friedman test to compare the three approaches (for both sequential and multi-task frameworks). We also applied corrections for multiple comparisons during the statistical analysis. Overall, we found statistical significant difference between our approach and the compared ones. This supports our previous discussions on

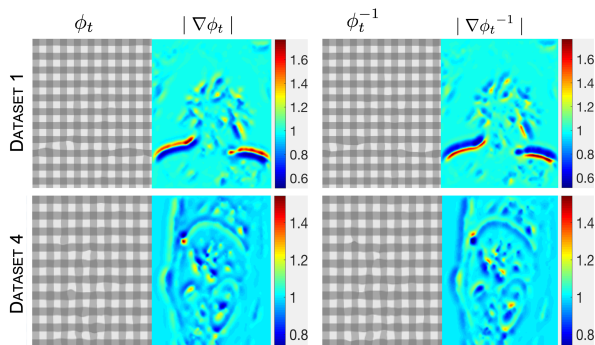


Figure C.8: Estimated motion and determinant maps of the deformation Jacobian for our proposed joint approach. This is shown for the transformation ϕ_i and its inverse ϕ_i^{-1} for two datasets (1 and 4).

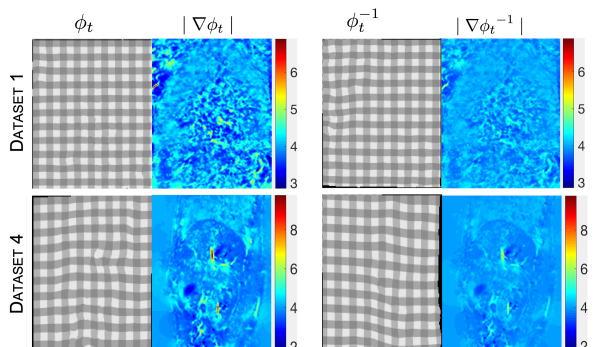


Figure C.9: Estimated motion and determinant maps of the deformation Jacobian for sequential approach based on hyperelastic registration. This is shown for the transformation ϕ_i and its inverse ϕ_i^{-1} for two datasets (1 and 4).

the ability of our model to offer the best reconstruction in comparison to the state of the art approaches for both sequential and joint models.

Appendix C. Further Visual Experiments

In this section, we extend the reconstruction comparisons from the main paper. In particular, for the sequential model we now include Datasets 2, 4 and 5. The results are displayed in Figs. C.11, C.12 and C.13 in which we observe that our joint approach successfully corrects for motion and aligns the different acquisitions resulting in a sharp reconstruction that contains very fine details, such as preserving the texture in the heart and vessels in the

liver and kidney. It further supports the finding from the main paper.

Moreover, we also provide further evaluation of our framework against other multi-task approaches (DC-CS Lingala et al. (2015) and GW-CS Royuela-del Val et al. (2016)). The reconstruction results are shown at Figs. C.11, C.12 and C.13. In a closer look at those reconstructions, one can observe that our approach produces very sharp reconstructions while preserving the texture in the relevant anatomical areas. This is validated for different acceleration factors. In contrast, DC-CS fails to carefully align the acquisition as we can see from the blurring artefacts around the edges. Additionally all the small details get blurred and smeared out. The GW-CS seems to perform reasonably well for fully-sampled data, however failing to remove the noise. This is accentuated at higher reduction factors, where the reconstructions contain significant noise which compromises the clinical interpretation of the images.

Moreover, we present for two datasets the estimated motion ϕ_i and its inverse ϕ_i^{-1} for a given time frame in Fig. C.8 for our proposed approach and in Fig. C.9 for the sequential approach based on hyperelastic regularisation. We can see that our proposed approach produces a reasonable estimation of the motion, where the motion fields are visualised by a deformation grid. Additionally, we show the corresponding Jacobian determinant maps for the deformations, in which the sequential approach based on hyperelastic regularisation was less robust than ours producing tiny areas (imperceptible) with large values. In these plots, we can see that the determinants remain positive meaning that our model ensures topology preservation both from a mathematical and practical point of view. The values are interpreted as follows: small deformations when values are closer to 1, big expansions when values are greater than 1, and big contractions when values are smaller than 1. Additionally, we can observe that the results for the sequential approach results in less smooth deformation and Jacobian determinants.

Sequential vs joint model. For further support of our experimental results section, we present additional visual results to compare our joint model to its corresponding sequential approach. However, we emphasise that performing the tasks sequentially will not yield to a final reconstruction that is directly comparable to ours. This is be-

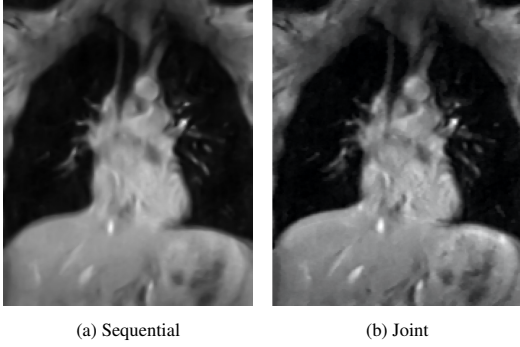


Figure C.10: Sequential vs joint approach for Dataset 1, using an acceleration factor of 4. The sequential experiment has been computed by performing first reconstruction of all slices, registration of all frames to a reference image (initialisation slice in the joint framework) and super-resolution of the mean registered slices. We use the same parameter setting as in the proposed joint approach. Even though the final reconstructions are not directly comparable as our joint framework seeks an optimal reconstruction not directly attributable to one specific measurement, we can observe the benefit of the joint modelling and optimisation. Our joint reconstruction preserves finer details and it is sharper compared to the sequential reconstruction.

cause our technique seeks for an optimal reconstruction not directly attributable to one specific measurement. The following experiment has been performed by decoupling the joint optimisation and performing reconstruction, registration and super-resolution in a sequential way. We use the same parameter setting as in the proposed joint approach and we choose as a reference for the registration the slice used for initialisation in the joint framework. In Fig. C.10, we show the results for the sequential approach obtained with the following pipeline: first we reconstruct all the frames, then we register them to one reference slice (chosen to be the same as the initialisation slice for the joint framework), finally we perform the super-resolution approach on the average image obtained by the registered slices. We can see that the sequential result is more blurry and loses fine details compared to the final reconstruction obtained with our joint framework. This further validates our multi-task approach and shows the significance of exploiting redundancy and complementary information to gain performance.

Appendix D. Further Mathematical Details

We recall the definition of the weighted BV-space and the associated weighted TV.

Definition Appendix D.1 (Baldi, 2001, Definition 2)). Let w be a weight function satisfying some properties (defined in Baldi (2001) and fulfilled by g_t). We denote by $BV_w(\Omega)$ the set of functions $f \in L^1(\Omega, w)$, which are integrable with respect to the measure $w(x)dx$, such that:

$$\sup \left\{ \int_{\Omega} f \operatorname{div}(\varphi) dx : |\varphi| \leq w \text{ e.}, \varphi \in Lip_0(\Omega, \mathbb{R}^2) \right\} < +\infty,$$

where $Lip_0(\Omega, \mathbb{R}^2)$ is the space of Lipschitz continuous functions with compact support. We denote by TV_w the previous quantity.

Notation: We introduce the space $BV_{g_t,0}(\Omega) = BV_0(\Omega) \cap BV_{g_t}(\Omega)$ (see (Demengel et al., 2012, Chapter 6.3.3) for more details on the trace operator on the space of functions with bounded variations) which will be used in the subsequent proof.

Appendix D.1. Detailed Proof of Theorem III.1

We report the detailed proof of Theorem 1 in Subsection 3.3 regarding the existence of minimisers.

The proof is based on arguments coming from the calculus of variations and is divided into three steps: derivation of a coercivity inequality, extraction of converging subsequences, and proof of the weak lower semicontinuity of the functional. We recall the assumptions on $g_t: \mathbb{R}^+ \rightarrow \mathbb{R}^+$, $g_t(0) = 1$, g_t is strictly decreasing, $\lim_{r \rightarrow +\infty} g_t(r) = 0$, and there exists $c > 0$ such that $c \leq g_t \leq 1$ everywhere. We also have $\phi_t: \bar{\Omega} \rightarrow \bar{\Omega}$ thanks to Ball's results (Ball (1981)) as seen later.

Coercivity inequality: We first have that

$$\mathcal{G}(0, (\operatorname{Id})_{t=1, \dots, T}) = 4a_1 \operatorname{meas}(\Omega) + \frac{1}{2T} \sum_{t=1}^T \|x_t\|_{L^2(\mathbb{R}^2)}^2 < +\infty.$$

Let $u \in BV(\Omega')$, $\phi_t \in \mathcal{W}$, $\forall t \in \{1, \dots, T\}$ such that $(Cu) \circ \phi_t^{-1} \in BV_{g_t,0}(\Omega)$, $\forall t \in \{1, \dots, T\}$, we then derive a

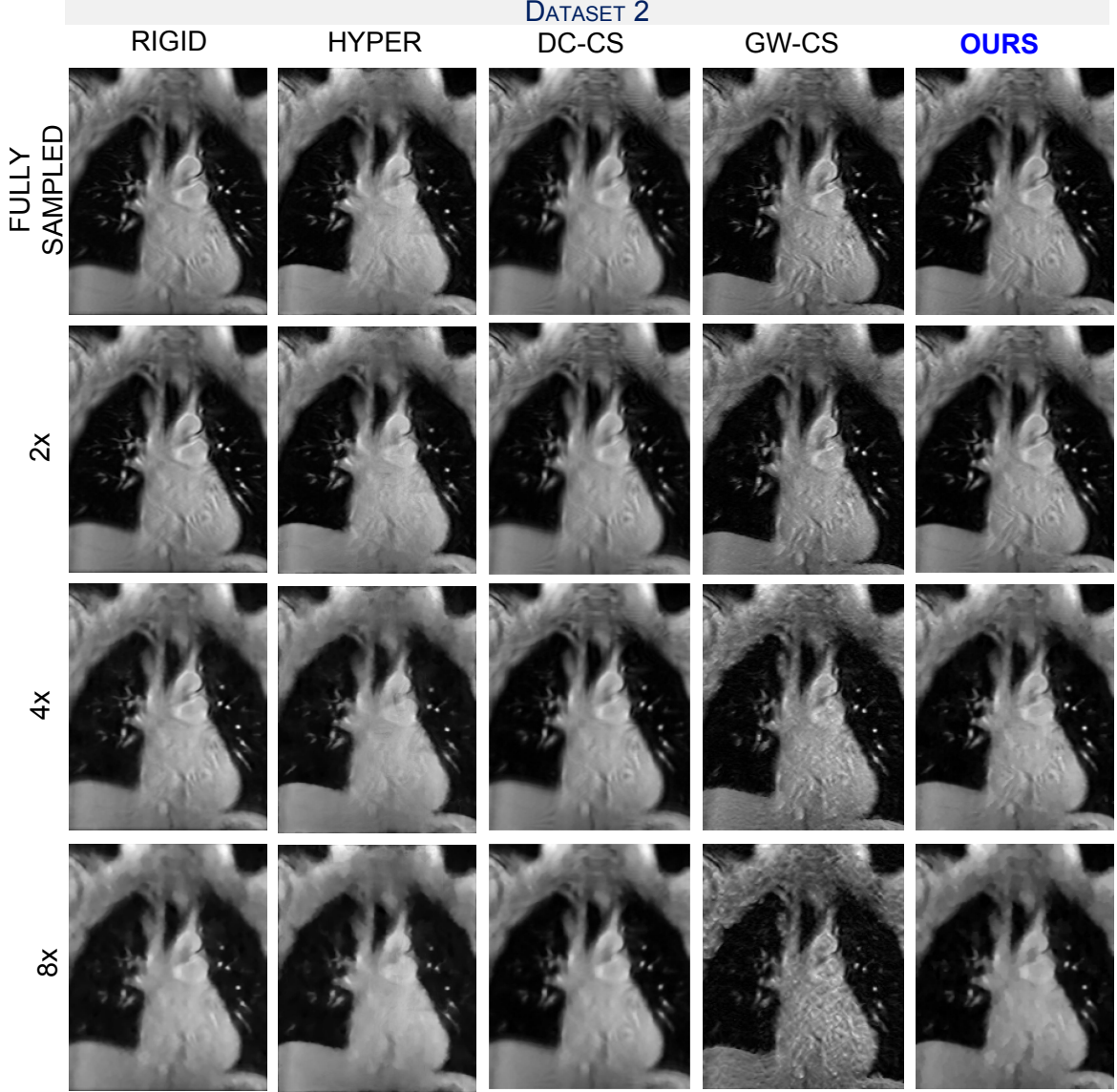


Figure C.11: Reconstruction results for Dataset 2 compared to sequential and joint approaches for different acceleration factors. Our proposed reconstruction preserves fine structures and better correct for motion, thus resulting in sharper edges compared to the other approaches reconstructions. The sequential results lose finer details. We can see that DC-CS results are very blurry and GW-CS very noisy. This is particularly accentuated for high undersampling factors.

coercivity inequality:

$$\begin{aligned}
\mathcal{G}(u, (\phi_t)_{t=1, \dots, T}) &\geq \frac{1}{T} \sum_{t=1}^T \left(a_1 \|\nabla \phi_t\|_{L^4(\Omega, \mathbb{R}^{2,2})}^4 \right. \\
&\quad \left. + \frac{a_2}{2} \|\det \nabla \phi_t\|_{L^4(\Omega)}^4 + \frac{a_2}{2} \left\| \frac{1}{\det \nabla \phi_t} \right\|_{L^4(\Omega)}^4 - 3a_2 \text{meas}(\Omega) \right. \\
&\quad \left. + \frac{1}{4C} \|(Cu) \circ \phi_t^{-1}\|_{L^2(\Omega)}^2 - \frac{1}{2} \|x_t\|_{L^2(\mathbb{R}^2)}^2 \right. \\
&\quad \left. + \delta \text{TV}_{g_t}((Cu) \circ \phi_t^{-1}) + \alpha \text{TV}(u) \right).
\end{aligned} \tag{19}$$

Indeed, $((Cu) \circ \phi_t^{-1}) \in BV_{g_t,0}(\Omega) \subset BV(\Omega) \subset L^2(\Omega)$ (Baldi (2001)) with continuous embedding, and $((Cu) \circ \phi_t^{-1})_e$ is the extension by 0 outside the domain Ω of $(Cu) \circ \phi_t^{-1}$,

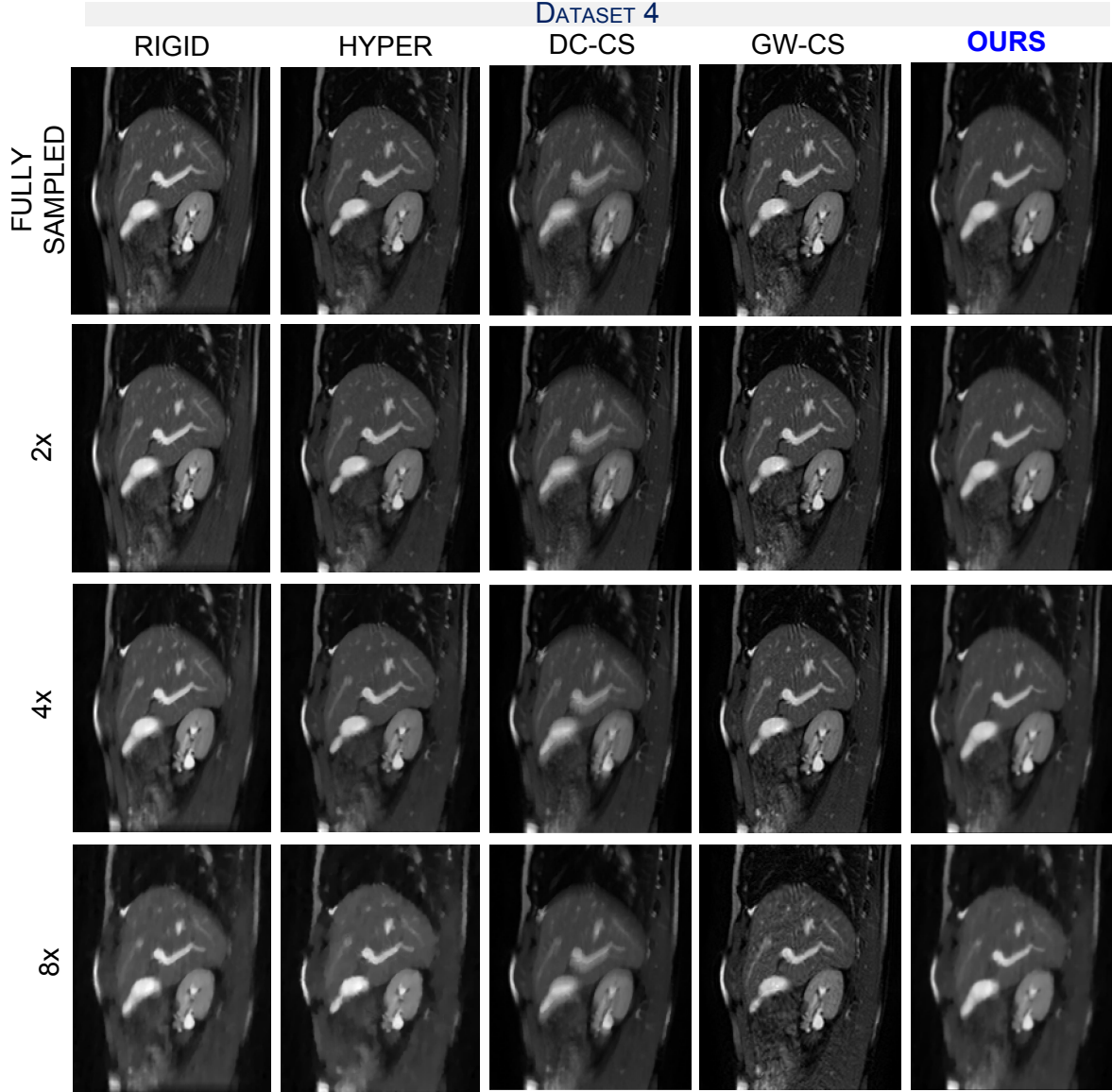


Figure C.12: Reconstruction results for Dataset 4 for different acceleration factors and different techniques in comparison to our proposed method. We can clearly see that our approach provides the best results in terms of sharp structures and fine texture, while the other joint models result to very blurry and noisy reconstructions (DC-CS and GW-CS). This is particularly accentuated for high undersampling factors.

then

$$\|((Cu) \circ \phi_t^{-1})_e\|_{L^2(\mathbb{R}^2)} = \|(Cu) \circ \phi_t^{-1}\|_{L^2(\Omega)} < +\infty,$$

and finally Plancherel's theorem and Banach-Schauder

theorem give us $\exists C > 0$

$$\begin{aligned} & \|\mathcal{A}((Cu) \circ \phi_t^{-1})_e\|_{L^2(\mathbb{R}^2)}^2 \\ & \geq \frac{1}{C} \|((Cu) \circ \phi_t^{-1})_e\|_{L^2(\mathbb{R}^2)}^2 = \frac{1}{C} \|(Cu) \circ \phi_t^{-1}\|_{L^2(\Omega)}^2. \end{aligned}$$

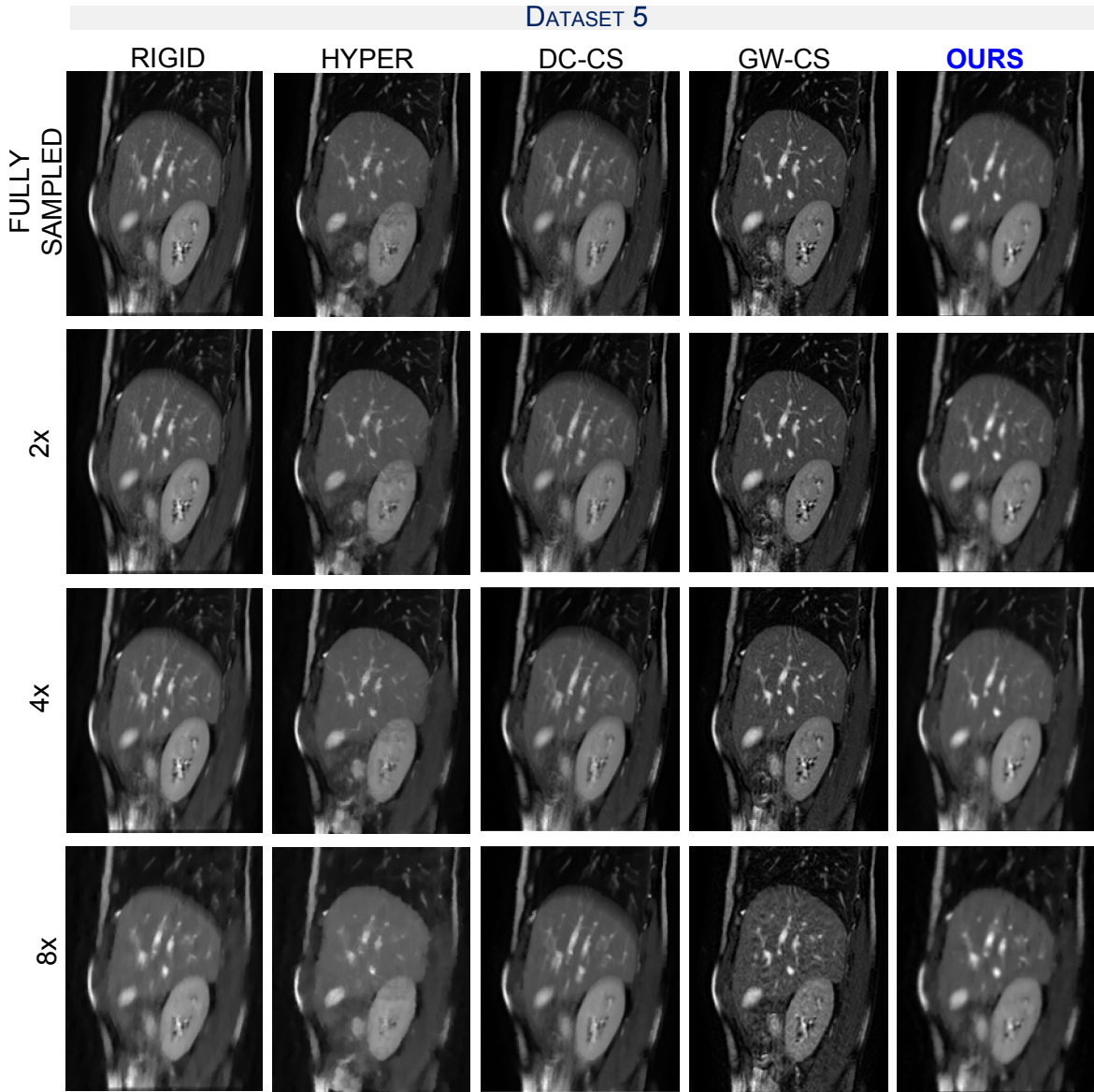


Figure C.13: Reconstruction results for Dataset 5 for different acceleration factors and different approaches including our proposed method. We can clearly see that our approach provides the best results in terms of sharp structures and fine texture, while DC-CS results very blurry and GW-CS very noisy. This is particularly accentuated for high undersampling factors.

The infimum is thus finite. In the following, let that $(u_n, (\phi_{t,n})_{t=1,\dots,T})_n \in \mathcal{U}$ be a minimising sequence such

$$\lim_{n \rightarrow +\infty} \mathcal{G}(u_n, (\phi_{t,n})_{t=1,\dots,T}) = \inf_{(u, (\phi_t)_{t=1,\dots,T}) \in \mathcal{U}} \mathcal{G}(u, (\phi_t)_{t=1,\dots,T}).$$

Extraction of converging subsequences: From the previous coercivity inequality and the finiteness of the infimum we deduce that:

- $(\phi_{t,n})_n$ is uniformly bounded according to n in $W^{1,4}(\Omega, \mathbb{R}^2)$ for each $t = 1, \dots, T$ by using the generalised Poincaré's inequality and the fact that $\phi_{t,n}$ is equal to the identity on the boundary $\partial\Omega$.
- $(\det\nabla\phi_{t,n})_n$ is uniformly bounded according to n in $L^4(\Omega)$ for each $t = 1, \dots, T$.
- $((Cu_n) \circ \phi_{t,n}^{-1})_n$ is uniformly bounded according to n in $BV_{g_t}(\Omega)$ and thus in $BV(\Omega)$ since $c \leq g_t \leq 1$ everywhere for each $t = 1, \dots, T$. Since $\phi_{t,n}$ are bi-Hölder homeomorphisms (see justification in the sequel), everything makes sense.

Therefore, we can extract subsequences (but for the sake of conciseness we keep the same notations) such that:

- $\phi_{t,n} \rightharpoonup \bar{\phi}_t$ in $W^{1,4}(\Omega, \mathbb{R}^2)$ for each $t = 1, \dots, T$ and by weak continuity of the trace operator, we deduce that $\bar{\phi}_t \in \text{Id} + W_0^{1,4}(\Omega, \mathbb{R}^2)$.
- $\det\nabla\phi_{t,n} \rightharpoonup \delta_t$ in $L^4(\Omega)$ for all $t = 1, \dots, T$.
- $(Cu_n) \circ \phi_{t,n}^{-1} \rightharpoonup \alpha_t$ in $L^q(\Omega)$ for $q \in [1, 2[$ and thus in $L^1(\Omega, g_t)$ with $\alpha_t \in BV(\Omega) \subset BV_{g_t}(\Omega)$. By continuity of the trace operator, we deduce that $\alpha_t \in BV_{g_t,0}(\Omega)$.
- $(Cu_n) \circ \phi_{t,n}^{-1} \rightharpoonup \alpha_t$ in $L^2(\Omega)$ for each $t = 1, \dots, T$ by uniqueness of the weak limit in $L^1(\Omega)$ and the continuous embedding of $L^2(\Omega) \subset L^1(\Omega)$. Also, since $\alpha_t \in BV_{g_t,0}(\Omega)$, we can extend it by 0 outside the domain Ω and we have $((Cu_n) \circ \phi_{t,n}^{-1})_e \rightharpoonup (\alpha_t)_e$ in $L^2(\mathbb{R}^2)$, for each $t = 1, \dots, T$.

Also, from [\(Dacorogna 2008, Theorem 8.20\)](#), we have that $\det\nabla\phi_{t,n} \rightharpoonup \det\nabla\bar{\phi}_t$ in $L^2(\Omega)$ for each $t = 1, \dots, T$, and by uniqueness of the weak limit in $L^2(\Omega)$ and the continuous embedding $L^4(\Omega) \subset L^2(\Omega)$, we deduce that $\delta_t = \det\nabla\bar{\phi}_t$ for each $t = 1, \dots, T$. Also, since we have

for $\tilde{q} = 2 + \frac{1}{2} > 2$:

$$\begin{aligned} & \int_{\Omega} \|(\nabla\phi_{t,n})^{-1}(x)\|_F^{\tilde{q}} \det\nabla\phi_{t,n}(x) dx \\ &= \int_{\Omega} \|\nabla\phi_{t,n}(x)\|_F^{\tilde{q}} (\det\nabla\phi_{t,n})^{1-\tilde{q}} dx \\ &\leq \|\nabla\phi_{t,n}\|_{L^4(\Omega, \mathbb{R}^{2,2})}^{\tilde{q}} \|(\det\nabla\phi_{t,n})^{-1}\|_{L^4(\Omega)}^{\tilde{q}-1}, \end{aligned}$$

using Hölder's inequality with $\tilde{p} = \frac{4}{\tilde{q}}$, $r = \frac{4}{\tilde{q}-1}$ and noticing that $\frac{4(\tilde{q}-1)}{4-\tilde{q}} = 4$. This quantity is uniformly bounded according to n for each t from what precedes and we deduce from [\(Ball, 1981, Theorem 1 and 2\)](#) that $(\phi_{t,n})$ are bi-Hölder homeomorphisms and therefore $\phi_{t,n}^{-1}$ exists.

Weak lower semi-continuity: As the inferior limit of a sum is always greater than the sum of inferior limits, we focus on each component independently. We first prove the strong lower semi-continuity of W_{Op} and then deduce its weak lower semi-continuity. In the sequel, we identify W_{Op} and \mathbb{W} and we recall its continuity and convexity. As for the deformation regularisation component, observe that if $\psi_n \rightarrow \bar{\psi}$ in $W^{1,4}(\Omega, \mathbb{R}^2)$, then $\nabla\psi_n \rightarrow \nabla\bar{\psi}$ in $L^4(\Omega, \mathbb{R}^{2,2})$ and we can extract a subsequence still denoted $(\nabla\psi_n)$ such that $\nabla\psi_n \rightarrow \nabla\bar{\psi}$ almost everywhere in Ω . If $\delta_n \rightarrow \bar{\delta}$ in $L^4(\Omega)$, then we can extract a subsequence still denoted (δ_n) such that $\delta_n \rightarrow \bar{\delta}$ almost everywhere in Ω . Then by continuity of W_{Op} , we get that $W_{Op}(\nabla\psi_n(x), \delta_n(x)) \rightarrow W_{Op}(\nabla\bar{\psi}(x), \bar{\delta}(x))$ almost everywhere in Ω . Then by applying Fatou's lemma, we have that

$$\liminf_{n \rightarrow +\infty} \int_{\Omega} W_{Op}(\nabla\psi_n(x), \delta_n(x)) dx \geq \int_{\Omega} W_{Op}(\nabla\bar{\psi}(x), \bar{\delta}(x)) dx.$$

Since W_{Op} is convex, so is $\int_{\Omega} W_{Op}(\xi(x), \delta(x)) dx$, and we can apply [\(Brezis, 1983, Corollaire III.8\)](#) to get that $\int_{\Omega} W_{Op}(\xi(x), \delta(x)) dx$ is weakly lower semicontinuous in $L^4(\Omega, \mathbb{R}^{2,2}) \times L^4(\Omega)$. We deduce that

$$\begin{aligned} & \liminf_{n \rightarrow +\infty} \int_{\Omega} W_{Op}(\nabla\phi_{t,n}(x), \det\nabla\phi_{t,n}(x)) dx \\ &\geq \int_{\Omega} W_{Op}(\nabla\bar{\phi}_t(x), \det\nabla\bar{\phi}_t(x)) dx. \end{aligned}$$

Also since $(Cu_n) \circ \phi_{t,n}^{-1} \rightharpoonup \alpha_t$ in $L^1(\Omega)$ and so in $L^1(\Omega, g_t)$, then by the semi-continuity theorem from [\(Baldi 2001, Theorem 3.2\)](#), we conclude that $\text{TV}_{g_t}(\alpha_t) \leq$

$\liminf_{n \rightarrow +\infty} \text{TV}_{g_t}((Cu_n) \circ \phi_{t,n}^{-1})$ for all $t = 1, \dots, T$.

\mathcal{A} is a linear operator and continuous for the strong topology from $L^2(\mathbb{R}^2)$ to $L^2(\mathbb{R}^2)$. Therefore, by applying (Brezis, 1983, Theorem III.9), \mathcal{A} is continuous from the weak topology of $L^2(\mathbb{R}^2)$ to the weak topology of $L^2(\mathbb{R}^2)$. As $((Cu_n) \circ \phi_{t,n}^{-1})_e \rightarrow (\alpha_t)_e$ in $L^2(\mathbb{R}^2)$, we deduce that $\mathcal{A}((Cu_n) \circ \phi_{t,n}^{-1})_e \rightarrow \mathcal{A}(\alpha_t)_e$ and thus $\mathcal{A}((Cu_n) \circ \phi_{t,n}^{-1})_e - x_t \rightarrow \mathcal{A}(\alpha_t)_e - x_t$ in $L^2(\mathbb{R}^2)$. By the weak lower semi-continuity of the norm, we deduce that $\liminf_{n \rightarrow +\infty} \|\mathcal{A}((Cu_n) \circ \phi_{t,n}^{-1})_e - x_t\|_{L^2(\mathbb{R}^2)}^2 \geq \|\mathcal{A}(\alpha_t)_e - x_t\|_{L^2(\mathbb{R}^2)}^2$.

We now need to prove that

$$(Cu_n) \circ \phi_{t,n}^{-1} \circ \phi_{t,n} = Cu_n \rightarrow \alpha_t \circ \bar{\phi}_t = \bar{U}_t$$

in $L^p(\Omega)$ for all $t = 1, \dots, T$. This allows us to show the convergence of (Cu_n) as a first step to prove the convergence of (u_n) and deduce the lower semi-continuity of the TV regulariser term. We recall that $p \in]1, \frac{8}{5}[$. We first have:

$$\begin{aligned} & \| (Cu_n) \circ \phi_{t,n}^{-1} \circ \phi_{t,n} - \alpha_t \circ \bar{\phi}_t \|_{L^p(\Omega)} \\ & \leq \| (Cu_n) \circ \phi_{t,n}^{-1} \circ \phi_{t,n} - \alpha_t \circ \phi_{t,n} \|_{L^p(\Omega)} \\ & \quad + \| \alpha_t \circ \phi_{t,n} - \alpha_t \circ \bar{\phi}_t \|_{L^p(\Omega)}. \end{aligned}$$

We now focus on the first term and make the change of variable $y = \phi_{t,n}(x) \Leftrightarrow x = \phi_{t,n}^{-1}(y)$ and $dy = \det \nabla \phi_{t,n}(x) dx$, $dx = \frac{1}{\det \nabla \phi_{t,n}(\phi_{t,n}^{-1}(y))} dy$ which is possible thanks to the results in (Ball, 1981):

$$\begin{aligned} & \int_{\Omega} |(Cu_n) \circ \phi_{t,n}^{-1} \circ \phi_{t,n} - \alpha_t \circ \phi_{t,n}|^p dx \\ & = \int_{\Omega} |(Cu_n) \circ \phi_{t,n}^{-1} - \alpha_t|^p \frac{1}{|\det \nabla \phi_{t,n}(\phi_{t,n}^{-1}(y))|} dy, \\ & \leq \| (Cu_n) \circ \phi_{t,n}^{-1} - \alpha_t \|_{L^{\frac{5p}{4}}(\Omega)}^p \left(\int_{\Omega} \frac{1}{|\det \nabla \phi_{t,n}(\phi_{t,n}^{-1}(y))|^5} dy \right)^{\frac{1}{5}}, \\ & \leq \| (Cu_n) \circ \phi_{t,n}^{-1} - \alpha_t \|_{L^{\frac{5p}{4}}(\Omega)}^p \left(\int_{\Omega} \frac{1}{|\det \nabla \phi_{t,n}(x)|^4} dx \right)^{\frac{1}{5}}, \end{aligned}$$

using Hölder's inequality and making another change of variable. Since $(Cu_n) \circ \phi_{t,n}^{-1} \rightarrow \alpha_t$ in $L^{\frac{5p}{4}}(\Omega)$, as $\frac{5p}{4} < 2$, and $\|\frac{1}{\det \nabla \phi_{t,n}}\|_{L^4(\Omega)}$ is uniformly bounded, we deduce that

$$\int_{\Omega} |(Cu_n) \circ \phi_{t,n}^{-1} \circ \phi_{t,n} - \alpha_t \circ \phi_{t,n}|^p dx \rightarrow 0.$$

According to (Demengel et al., 2012, Theorem 6.70), there exists a sequence $(\xi_t^k)_k$ of functions in $C_c^\infty(\Omega)$ such that $\|\alpha_t - \xi_t^k\|_{L^1(\Omega)} \rightarrow 0$ and $\int_{\Omega} |\nabla \xi_t^k| \rightarrow \int_{\Omega} |\nabla \alpha_t| + \int_{\partial\Omega} |\alpha_t| dx$ with $\int_{\partial\Omega} |\alpha_t| dx = 0$ since $\alpha_t = 0$ on $\partial\Omega$, for all $t = 1, \dots, T$. Thus (ξ_t^k) is uniformly bounded according to k in $BV(\Omega) \subset L^q(\Omega)$, for $q \in [1, 2[$, and therefore up to a subsequence $\xi_t^k \rightarrow \alpha_t$ in $L^q(\Omega)$ for $q \in [1, 2[$. Let $\varepsilon > 0$ and thus we fix $N \in \mathbb{N}^*$ such that $\|\xi_t^N - \alpha_t\|_{L^{\frac{5p}{4}}(\Omega)} \leq \varepsilon$. We now have:

$$\begin{aligned} & \| \alpha_t \circ \phi_{t,n} - \alpha_t \circ \bar{\phi}_t \|_{L^p(\Omega)} \leq \| \alpha_t \circ \phi_{t,n} - \xi_t^N \circ \phi_{t,n} \|_{L^p(\Omega)} \\ & \quad + \| \xi_t^N \circ \phi_{t,n} - \xi_t^N \circ \bar{\phi}_t \|_{L^p(\Omega)} + \| \xi_t^N \circ \bar{\phi}_t - \alpha_t \circ \bar{\phi}_t \|_{L^p(\Omega)}, \\ & \leq \left(\int_{\Omega} |\alpha_t - \xi_t^N|^p \frac{1}{|\det \nabla \phi_{t,n}(\phi_{t,n}^{-1}(y))|} dy \right)^{\frac{1}{p}} \\ & \quad + L_\varepsilon \| \phi_{t,n} - \bar{\phi}_t \|_{L^p(\Omega, \mathbb{R}^2)} \\ & \quad + \left(\int_{\Omega} |\xi_t^N - \alpha_t|^p \frac{1}{|\det \nabla \bar{\phi}_t(\bar{\phi}_t^{-1}(y))|} dy \right)^{\frac{1}{p}}, \end{aligned}$$

with L_ε denoting the Lipschitz constant of ξ_t^N , and using a change of variable possible since ϕ_t is bi-Hölder homeomorphism using the same arguments as previously. As $\phi_{t,n} \rightarrow \bar{\phi}_t$ in $W^{1,4}(\Omega) \subset L^p(\Omega, \mathbb{R}^2)$, there exists $K \in \mathbb{N}^*$ such that for any $n \geq K$, $\|\phi_{t,n} - \bar{\phi}_t\|_{L^p(\Omega, \mathbb{R}^2)} \leq \frac{\varepsilon}{L_\varepsilon}$. From now on, we assume n satisfies $n \geq K$, and we use Hölder's inequality:

$$\begin{aligned} & \| \alpha_t \circ \phi_{t,n} - \alpha_t \circ \bar{\phi}_t \|_{L^p(\Omega)} \leq \| \alpha_t - \xi_t^N \|_{L^{\frac{5p}{4}}(\Omega)} \\ & \quad \left(\int_{\Omega} \frac{1}{|\det \nabla \phi_{t,n}(\phi_{t,n}^{-1}(y))|^5} dy \right)^{\frac{1}{5}} + \varepsilon \\ & \quad + \| \xi_t^N - \alpha_t \|_{L^{\frac{5p}{4}}(\Omega)} \left(\int_{\Omega} \frac{1}{|\det \nabla \bar{\phi}_t(\bar{\phi}_t^{-1}(y))|^5} dy \right)^{\frac{1}{5}}, \\ & \leq \varepsilon \| (\det \nabla \phi_{t,n})^{-1} \|_{L^4(\Omega)}^{\frac{4}{5p}} + \varepsilon + \varepsilon \| (\det \nabla \bar{\phi}_t)^{-1} \|_{L^4(\Omega)}^{\frac{4}{5p}}, \end{aligned}$$

with $\| \det \nabla \phi_{t,n}^{-1} \|_{L^4(\Omega)}$ uniformly bounded according to n and $\| (\det \nabla \bar{\phi}_t)^{-1} \|_{L^4(\Omega)}$ bounded from what precedes. So by letting ε tend to 0, we obtain that $\int_{\Omega} \| \alpha_t \circ \phi_{t,n} - \alpha_t \circ \bar{\phi}_t \|^p dx \rightarrow 0$ and consequently

$$(Cu_n) \circ \phi_{t,n}^{-1} \circ \phi_{t,n} = Cu_n \rightarrow \alpha_t \circ \bar{\phi}_t$$

for all $t = 1, \dots, N$ in $L^p(\Omega)$. By uniqueness of the limit, we have that $\bar{U}_t = \alpha_t \circ \bar{\phi}_t \Leftrightarrow \alpha_t = \bar{U}_t \circ \bar{\phi}_t^{-1}$

for all $t = 1, \dots, T$ in $L^p(\Omega)$, with $\bar{U}_t \in L^p(\Omega)$ and $\bar{U}_t \circ \bar{\phi}_t^{-1} \in BV_{g_t,0}(\Omega)$.

Now, we set $\tilde{u}_n = \frac{1}{|\Omega'|} \int_{\Omega'} u_n dx$, and $u_{0,n} = u_n - \tilde{u}_n$. We clearly have $\int_{\Omega'} u_{0,n} dx = 0$ for all n , and $\text{TV}(u_{0,n}) = \text{TV}(u_n)$ is uniformly bounded thanks to the coercivity inequality. We denote this uniform bound by ν . Thus using Poincaré-Wirtinger's inequality we obtain

$$\|u_{0,n}\|_{L^1(\Omega')} \leq c_1 \text{TV}(u_{0,n}) \leq c_1 \nu,$$

with $c_1 > 0$. We now need a bound for $\|C\tilde{u}_n\|_{L^p(\Omega)}$:

$$\begin{aligned} & \|C\tilde{u}_n\|_{L^p(\Omega)}^2 - 2\|C\tilde{u}_n\|_{L^p(\Omega)}\|C\|_{\mathcal{L}(L^1(\Omega'),L^p(\Omega))}\|u_{0,n}\|_{L^1(\Omega')} \\ & \leq \|C\tilde{u}_n\|_{L^p(\Omega)}^2 - 2\|C\tilde{u}_n\|_{L^p(\Omega)}\|Cu_{0,n}\|_{L^p(\Omega)}, \\ & \leq (\|C\tilde{u}_n\|_{L^p(\Omega)} - \|Cu_{0,n}\|_{L^p(\Omega)})^2, \\ & \leq \|C(\tilde{u}_n + u_{0,n})\|_{L^p(\Omega)}^2, \\ & \leq \|Cu_n\|_{L^p(\Omega)}^2 \leq c_2^2 < +\infty, \text{ for some } c_2 \in \mathbb{R} \end{aligned}$$

as (Cu_n) strongly converges in $L^p(\Omega)$. Besides, we have $\|C\|_{\mathcal{L}(L^1(\Omega'),L^p(\Omega))}\|u_{0,n}\|_{L^1(\Omega')} \leq \|C\|_{\mathcal{L}(L^1(\Omega'),L^p(\Omega))}c_1\nu =: c_3 < +\infty$ and thus

$$\begin{aligned} \|C\tilde{u}_n\|_{L^p(\Omega)} &= \frac{1}{|\Omega'|} \left| \int_{\Omega'} u_n dx \right| \|C\mathbb{1}\|_{L^p(\Omega)} \\ &\leq 2\sqrt{c_3^2 + c_2^2}. \end{aligned}$$

Since $C\mathbb{1} \neq 0$, we have $\frac{1}{|\Omega'|} \left| \int_{\Omega'} u_n dx \right| \leq \frac{2\sqrt{c_3^2 + c_2^2}}{\|C\mathbb{1}\|_{L^p(\Omega)}} = c_4 < +\infty$. We therefore have

$$\begin{aligned} \|u_n\|_{L^1(\Omega')} &\leq \left\| u_{0,n} + \frac{1}{|\Omega'|} \int_{\Omega'} u_n dx \right\|_{L^1(\Omega')}, \\ &\leq \|u_{0,n}\|_{L^1(\Omega')} + \left| \int_{\Omega'} u_n dx \right|, \\ &\leq c_1\nu + c_4|\Omega'| < +\infty. \end{aligned}$$

Thus (u_n) is uniformly bounded according to n in $BV(\Omega')$ and there exists a subsequence still denoted (u_n) such that $u_n \rightarrow \bar{u}$ in $L^1(\Omega')$ with $\bar{u} \in BV(\Omega')$. By continuity of the operator C and the uniqueness of the limit, we deduce that $Cu_n \rightarrow C\bar{u} = \bar{U}_t$ in $L^p(\Omega)$ for all $t = 1, \dots, T$ and thus the dependency on t vanishes. By the semi-continuity theorem, we get

$$\text{TV}(\bar{u}) \leq \liminf_{n \rightarrow +\infty} \text{TV}(u_n)$$

By combining all the results, we obtain that

$$\begin{aligned} +\infty &> \inf_{(u,(\phi_t)_{t=1,\dots,T}) \in \mathcal{U}} \mathcal{G}(u, (\phi_t)_{t=1,\dots,T}) \\ &= \liminf_{n \rightarrow +\infty} \mathcal{G}(u_n, (\phi_{t,n})_{t=1,\dots,T}) \\ &\geq \frac{1}{T} \sum_{t=1}^T \delta \text{TV}_{g_t}((C\bar{u}) \circ \bar{\phi}_t^{-1}) + \frac{1}{2} \|\mathcal{A}((C\bar{u}) \circ \bar{\phi}_t^{-1})_e - x_t\|_{L^2(\mathbb{R}^2)}^2 \\ &\quad + \int_{\Omega} W_{Op}(\nabla \bar{\phi}_t) dx + \alpha \text{TV}(\bar{u}). \end{aligned}$$

It thus means that $\det \nabla \bar{\phi}_t \in L^4(\Omega)$, $(\det \nabla \bar{\phi}_t)^{-1} \in L^4(\Omega)$, and $\det \nabla \bar{\phi}_t > 0$ almost everywhere in Ω for all $t = 1, \dots, T$. Indeed, since $W_{Op}(\nabla \bar{\phi}_t(x), \det \nabla \bar{\phi}_t(x)) = +\infty$ when $\det \nabla \bar{\phi}_t(x) \leq 0$, it means that the set on which it happens must be of null measure otherwise we would have $\int_{\Omega} W_{Op}(\nabla \bar{\phi}_t, \det \nabla \bar{\phi}_t) dx = +\infty$. Also, by applying the same reasoning for each $\phi_{t,n}$, we prove that $\bar{\phi}_t$ is a bi-Hölder homeomorphism and have that $\bar{\phi}_t \in \mathcal{W}$ for each $t = 1, \dots, T$.

We thus have proved the existence of minimisers for our problem (4).

References

- Adluru, G., DiBella, E.V., Schabel, M.C., 2006. Model-based registration for dynamic cardiac perfusion MRI. *J Magn Reson Imaging*; 24(5):1062-70 .
- Andre, J.B., Bresnahan, B.W., Mossa-Basha, M., Hoff, M.N., Smith, C.P., Anzai, Y., Cohen, W.A., 2015. Toward quantifying the prevalence, severity, and cost associated with patient motion during clinical MR examinations. *Journal of the American College of Radiology* 12, 689–695.
- Aviles-Rivero, A.I., Williams, G., Graves, M.J., Schönlieb, C.B., 2018. Compressed sensing plus motion (CS+M): A new perspective for improving undersampled MR image reconstruction. *arXiv preprint arXiv:1810.10828* .
- Baldi, A., 2001. Weighted BV functions. *Houston J. Math.* 27, 683–705.

- Ball, J.M., 1981. Global invertibility of Sobolev functions and the interpenetration of matter. *Proceedings of the Royal Society of Edinburgh: Section A Mathematics* 88, 315–328.
- Baumgartner, C.F., Kolbitsch, C., McClelland, J.R., Rueckert, D., King, A.P., 2017. Autoadaptive motion modelling for MR-based respiratory motion estimation. *Med Image Anal* 35, 83 – 100.
- Birn, R.M., Cox, R.W., Bandettini, P.A., 2004. Experimental designs and processing strategies for fMRI studies involving overt verbal responses. *Neuroimage* 23, 1046–1058.
- Blume, M., Martinez-Moller, A., Keil, A., Navab, N., Rafecas, M., 2010. Joint reconstruction of image and motion in gated positron emission tomography. *IEEE Trans Med Imaging* 29, 1892–1906.
- Brezis, H., 1983. *Analyse fonctionnelle*. Collection Mathématiques appliquées pour la maîtrise.
- Brown, M.A., Semelka, R.C., Dale, B.M., 2015. *MRI: basic principles and applications*. John Wiley & Sons.
- Burger, M., Dirks, H., Schönlieb, C.B., 2018. A variational model for joint motion estimation and image reconstruction. *SIAM J. Imaging Sciences*, 11, 1, pp. 94–128 .
- Carmi, E., Liu, S., Alon, N., Fiat, A., Fiat, D., 2006. Resolution enhancement in MRI. *Magnetic resonance imaging* 24, 133–154.
- Chambolle, A., 2004. An algorithm for total variation minimization and applications. *J Math Imaging Vis* 20, 89–97.
- Chambolle, A., Pock, T., 2011. A first-order primal-dual algorithm for convex problems with applications to imaging. *J Math Imaging Vis* 40: 120 .
- Chaudhari, A.S., Fang, Z., Kogan, F., Wood, J., Stevens, K.J., Gibbons, E.K., Lee, J.H., Gold, G.E., Hargreaves, B.A., 2018. Super-resolution musculoskeletal MRI using deep learning. *Magnetic resonance in medicine* 80, 2139–2154.
- Christensen, G.E., Rabbitt, R.D., Miller, M.I., 1996. Deformable templates using large deformation kinematics. *IEEE Trans Image Process* 5, 1435–1447.
- Chun, S., Fessler, J., . Joint image reconstruction and nonrigid motion estimation with a simple penalty that encourages local invertibility. *Proc SPIE* 7258.
- Corona, V., Aviles-Rivero, A., Debroux, N., M.Grave, Guyader, C.L., Schoenlieb, C.B., Williams, G., 2019. Multi-tasking to correct: motion-compensated MRI via joint reconstruction and registration. *Scale Space and Variational Methods in Computer Vision LNCS conference proceedings*, Springer. .
- Dacorogna, B., 2008. *Direct Methods in the Calculus of Variations*, Second Edition. Springer.
- Demengel, F., Demengel, G., Ern , R., 2012. *Functional Spaces for the Theory of Elliptic Partial Differential Equations*. Universitext, Springer London.
- Ehrhardt, M.J., Betcke, M.M., 2016. Multi-contrast MRI reconstruction with structure-guided total variation. *SIAM Journal on Imaging Sciences* 9, 1084–1106. URL: <http://arxiv.org/abs/1511.06631><http://epubs.siam.org/doi/10.1137/15M1047325>, doi:10.1137/15M1047325, arXiv:1511.06631.
- Fessler, J.A., 2010. Optimization transfer approach to joint registration/reconstruction for motion-compensated image reconstruction. *ISBI* .
- Fogtman, M., Seshamani, S., Kim, K., Chapman, T., Studholme, C., 2012. A unified approach for motion estimation and super resolution reconstruction from structural magnetic resonance imaging on moving subjects, in: *MICCAI Workshop on Perinatal and Paediatric Imaging*, Nice: PaPI. pp. 9–16.
- George, R., Chung, T.D., Vedam, S.S., Ramakrishnan, V., Mohan, R., Weiss, E., Keall, P.J., 2006. Audio-visual biofeedback for respiratory-gated radiotherapy: Impact of audio instruction and audio-visual biofeedback on respiratory-gated radiotherapy. *International Journal of Radiation Oncology*Biophysics* 65, 924 – 933.
- Greenspan, H., Oz, G., Kiryati, N., Peled, S., 2002. MRI inter-slice reconstruction using super-resolution. *Magnetic Resonance Imaging* 20, 437–446.

- Gris, B., Chen, C., Ozan, , 2019. Image reconstruction through metamorphosis. *Inverse Problems* 36. doi:[10.1088/1361-6420/ab5832](https://doi.org/10.1088/1361-6420/ab5832).
- Gudbjartsson, H., Patz, S., 1995. The rician distribution of noisy MRI data. *Magnetic resonance in medicine* 34, 910–914.
- Gupta, S.N., Solaiyappan, M., Beache, G.M., Arai, A.E., Foo, T.K., 2003. Fast method for correcting image misregistration due to organ motion in time-series MRI data. *Magn Reson Med* 49, 506–514.
- Havsteen, I., Ohlhues, A., Madsen, K.H., Nybing, J.D., Christensen, H., Christensen, A., 2017. Are movement artifacts in magnetic resonance imaging a real problem?— A narrative review. *Frontiers in neurology* 8, 232.
- He, Y., Yap, K.H., Chen, L., Chau, L.P., 2007. A non-linear least square technique for simultaneous image registration and super-resolution. *IEEE transactions on image processing : a publication of the IEEE Signal Processing Society* 16, 2830–41. doi:[10.1109/TIP.2007.908074](https://doi.org/10.1109/TIP.2007.908074).
- Hoisak, J.D., Sixel, K.E., Tirona, R., Cheung, P.C., Pignol, J.P., 2006. Prediction of lung tumour position based on spirometry and on abdominal displacement: Accuracy and reproducibility. *Radiotherapy and Oncology* 78, 339 – 346. doi:<https://doi.org/10.1016/j.radonc.2006.01.008>.
- Jacobson, M., Fessler, J., 2003. Joint estimation of image and deformation parameters in motion-corrected PET, in: *IEEE NSS Conf*, pp. 3290–3294.
- Jansen, M., Kuijff, H., Veldhuis, W., Wessels, F., Van Leeuwen, M., Pluim, J., 2017. Evaluation of motion correction for clinical dynamic contrast enhanced MRI of the liver. *Physics in Medicine & Biology* 62, 7556.
- Jiang, S.B., 2006. Technical aspects of image-guided respiration-gated radiation therapy. *Medical Dosimetry* 31, 141 – 151.
- Johansson, A., Balter, J., Cao, Y., 2018. Rigid-body motion correction of the liver in image reconstruction for golden-angle stack-of-stars DCE MRI. *Magn Reson Med* 79, 1345–1353.
- Kaji, S., Yang, P.C., Kerr, A.B., Tang, W.W., Meyer, C.H., Macovski, A., Pauly, J.M., Nishimura, D.G., Hu, B.S., 2001. Rapid evaluation of left ventricular volume and mass without breath-holding using real-time interactive cardiac magnetic resonance imaging system. *Journal of the American College of Cardiology* 38, 527–533.
- Keall, P.J., Kini, V.R., Vedam, S.S., Mohan, R., 2000. Motion adaptive x-ray therapy: a feasibility study. *Physics in Medicine and Biology* 46, 1–10.
- Ledesma-Carbayo, M.J., Kellman, P., Arai, A.E., McVeigh, E.R., 2007. Motion corrected free-breathing delayed-enhancement imaging of myocardial infarction using nonrigid registration. *J Magn Reson Imaging*. 2007;26(1):184-90 .
- Ledesma-Carbayo MJ, Kellman P, H.L.A.A.M.E., 2007. Motion corrected free-breathing delayed-enhancement imaging of myocardial infarction using nonrigid registration. *J Magn Reson Imaging* 26, 184–90.
- Li, Z., Tielbeek, J.A., Caan, M.W., Puylaert, C.A., Ziech, M.L., Nio, C.Y., Stoker, J., van Vliet, L.J., Vos, F.M., 2015. Expiration-phase template-based motion correction of free-breathing abdominal dynamic contrast enhanced MRI. *IEEE TBE* 62, 1215–1225.
- Liang, Z.P., 2007. Spatiotemporal imaging with partially separable functions, in: *IEEE International Symposium on Biomedical Imaging: From Nano to Macro*, pp. 988–991.
- Lingala, S.G., DiBella, E., Jacob, M., 2015. Deformation corrected compressed sensing (DC-CS): A novel framework for accelerated dynamic MRI. *IEEE Trans Med Imaging* 34, 72–85.
- Lingala, S.G., Hu, Y., DiBella, E., Jacob, M., 2011a. Accelerated dynamic MRI exploiting sparsity and low-rank structure: kt SLR. *IEEE Trans Med Imaging* , 1042–1054.
- Lingala, S.G., Hu, Y., DiBella, E., Jacob, M., 2011b. Accelerated dynamic MRI exploiting sparsity and low-rank structure: kt SLR. *IEEE Trans Med Imaging* 30, 1042–1054.

- Lustig, M., Donoho, D., Pauly, J.M., 2007. Sparse MRI: The application of compressed sensing for rapid MR imaging. *Magn Reson Med* , 1182–1195.
- Mair, B.A., Gilland, D.R., Sun, J., 2006. Estimation of images and nonrigid deformations in gated emission CT. *IEEE Trans Med Imaging* 25, 1130–1144.
- Majumdar, A., Ward, R.K., 2012. Exploiting rank deficiency and transform domain sparsity for MR image reconstruction. *Magn Reson Imaging* , 9–18.
- Modersitzki, J., 2009. FAIR: Flexible Algorithms for Image Registration. SIAM, Philadelphia.
- Odille, F., Bustin, A., Chen, B., Vuissoz, P.A., Felblinger, J., 2015. Motion-corrected, super-resolution reconstruction for high-resolution 3D cardiac cine MRI, in: *International Conference on Medical Image Computing and Computer-Assisted Intervention (MICCAI)*, pp. 435–442.
- Odille, F., Menini, A., Escanyé, J.M., Vuissoz, P.A., Marie, P.Y., Beaumont, M., Felblinger, J., 2016. Joint reconstruction of multiple images and motion in MRI: Application to free-breathing myocardial T2 quantification. *IEEE Trans Med Imaging* 35, 197–207.
- Otazo, R., Candès, E., Sodickson, D.K., 2015. Low-rank plus sparse matrix decomposition for accelerated dynamic MRI with separation of background and dynamic components. *Magn Reson Med* , 1125–1136.
- Patel, V., Arocha, J.F., Kaufman, D., 1994. Diagnostic reasoning and medical expertise. *Psychology of learning and motivation-advances in research and theory* 31, 187–252.
- Peled, S., Yeshurun, Y., 2001. Superresolution in MRI: application to human white matter fiber tract visualization by diffusion tensor imaging. *Magnetic Resonance in Medicine* 45, 29–35.
- Plein, S., Smith, W.H., Ridgway, J.P., Kassner, A., Beacock, D.J., Bloomer, T.N., Sivananthan, M.U., . Qualitative and quantitative analysis of regional left ventricular wall dynamics using real-time magnetic resonance imaging: comparison with conventional breath-hold gradient echo acquisition in volunteers and patients. *J Magn Reson Imaging* .
- Plenge, E., Poot, D.H., Bernsen, M., Kotek, G., Houston, G., Wielopolski, P., van der Weerd, L., Niessen, W.J., Meijering, E., 2012. Super-resolution methods in MRI: Can they improve the trade-off between resolution, signal-to-noise ratio, and acquisition time? *Magnetic Reson Med* 68, 1983–1993.
- Ravishankar, S., Ye, J.C., Fessler, J.A., 2019. Image reconstruction: From sparsity to data-adaptive methods and machine learning. *arXiv preprint arXiv:1904.02816* .
- Rousseau, F., Glenn, O.A., Iordanova, B., Rodriguez-Carranza, C., Vigneron, D.B., Barkovich, J.A., Studholme, C., 2006. Registration-based approach for reconstruction of high-resolution in utero fetal MR brain images. *Academic radiology* 13, 1072–1081.
- Rudin, L.I., Osher, S., Fatemi, E., 1992. Nonlinear total variation based noise removal algorithms. *Physica D*, vol. 60, pp. 259-268 .
- Sachs, T.S., Meyer, C.H., Irarrazabal, P., Hu, B.S., Nishimura, D.G., Macovski, A., 1995. The diminishing variance algorithm for real-time reduction of motion artifacts in MRI. *Magn Reson Med* 34, 412–422.
- Scheffler, K., 2002. Superresolution in MRI? *Magnetic Resonance in Medicine: An Official Journal of the International Society for Magnetic Resonance in Medicine* 48, 408–408.
- Schumacher, H., Modersitzki, J., Fischer, B., 2009. Combined reconstruction and motion correction in SPECT imaging. *ITNS* 56, (1), pp. 73–80 .
- Setser, R.M., Fischer, S.E., Lorenz, C.H., 2000. Quantification of left ventricular function with magnetic resonance images acquired in real time. *J Magn Reson Imaging* 12, 430–438.
- von Siebenthal, M., Szekeely, G., Gamper, U., Boesiger, P., Lomax, A., Cattin, P., 2007. 4D MR imaging of respiratory organ motion and its variability. *Physics in Medicine & Biology* 52, 1547.
- Royuela-del Val, J., Cordero-Grande, L., Simmross-Wattenberg, F., Martín-Fernández, M., Alberola-López, C., 2016. Nonrigid groupwise registration for

- motion estimation and compensation in compressed sensing reconstruction of breath-hold cardiac cine MRI. *Magn Reson Med* 75, 1525–1536.
- de Vos, B.D., Berendsen, F.F., Viergever, M.A., Staring, M., Išgum, I., 2017. End-to-end unsupervised deformable image registration with a convolutional neural network, in: *DLMIA*, pp. 204–212.
- Wong, K.K., Yang, E.S., Wu, E.X., Tse, H.F., Wong, S.T., 2008. First-pass myocardial perfusion image registration by maximization of normalized mutual information. *JMRI* 27, 529–537.
- Yang, X., Kwitt, R., Styner, M., Niethammer, M., 2017. Quicksilver: Fast predictive image registration—a deep learning approach. *NeuroImage* 158, 378–396.
- Yue, L., Shen, H., Li, J., Yuan, Q., Zhang, H., Zhang, L., 2016. Image super-resolution: The techniques, applications, and future. *Signal Processing* 128, 389 – 408.
- Zaitsev, M., Maclaren, J., Herbst, M., 2015. Motion artifacts in MRI: a complex problem with many partial solutions. *J Magn Reson Imaging*, 42.
- Zhang, T., Pauly, J.M., Levesque, I.R., 2015. Accelerating parameter mapping with a locally low rank constraint. *Magn Reson Med* 73, 655–661.
- Zhang, X., Lam, E.Y., Wu, E.X., Wong, K.K., 2007. Application of Tikhonov regularization to super-resolution reconstruction of brain MRI images, in: *International Conference on Medical Imaging and Informatics*, pp. 51–56.